

# On the Origin of the Extracellular Action Potential Waveform: A Modeling Study

Carl Gold,<sup>1</sup> Darrell A. Henze,<sup>2</sup> Christof Koch,<sup>1</sup> and György Buzsáki<sup>3</sup>

<sup>1</sup>Computation and Neural Systems, California Institute of Technology, Pasadena, California; <sup>2</sup>Merck Research Laboratories, West Point, Pennsylvania; and <sup>3</sup>Center for Molecular and Behavioral Neuroscience, Rutgers University, Newark, New Jersey

Submitted 19 September 2005; accepted in final form 24 January 2006

**Gold, Carl, Darrell A. Henze, Christof Koch, and György Buzsáki.** On the origin of the extracellular action potential waveform: a modeling study. *J Neurophysiol* 95: 3113–3128, 2006. First published February 8, 2006; doi:10.1152/jn.00979.2005. Although extracellular unit recording is typically used for the detection of spike occurrences, it also has the theoretical ability to report about what are typically considered intracellular features of the action potential. We address this theoretical ability by developing a model system that captures features of experimentally recorded simultaneous intracellular and extracellular recordings of CA1 pyramidal neurons. We use the line source approximation method of Holt and Koch to model the extracellular action potential (EAP) voltage resulting from the spiking activity of individual neurons. We compare the simultaneous intracellular and extracellular recordings of CA1 pyramidal neurons recorded in vivo with model predictions for the same cells reconstructed and simulated with compartmental models. The model accurately reproduces both the waveform and the amplitude of the EAPs, although it was difficult to achieve simultaneous good matches on both the intracellular and extracellular waveforms. This suggests that accounting for the EAP waveform provides a considerable constraint on the overall model. The developed model explains how and why the waveform varies with electrode position relative to the recorded cell. Interestingly, each cell's dendritic morphology had very little impact on the EAP waveform. The model also demonstrates that the varied composition of ionic currents in different cells is reflected in the features of the EAP.

## INTRODUCTION

Extracellular action potential (EAP) recordings form one of the primary means for studying the activity of the intact brain. Multielectrode arrays and spike-sorting algorithms have advanced to the point where hundreds of neurons can be reliably recorded in a single experiment (e.g., see Csicsvari et al. 2003; Wilson and McNaughton 1993). Typically, EAP recordings are used only to determine whether and when neurons have spiked, under the assumption that the actual waveform of individual EAPs does not convey any information. At the same time, average EAP waveforms are known to exhibit a range of characteristic features when observed on a millisecond time-scale, and these variations can be used to distinguish between different neuronal classes (Csicsvari et al. 1999; Mountcastle et al. 1969) as well as individual neurons within classes (e.g., Quian Quiroga et al. 2004). However, there have been few attempts to systematically study the causes of the variability in EAP waveforms either through experimental work or through computer modeling (Buzsáki et al. 1996; Holt and Koch 1999;

Moffitt and McIntyre 2005; Quirk et al. 2001; Rall 1962). The paucity of studies probably results from both insufficient data and inadequate techniques with which to model EAPs in a meaningful way. It is generally assumed that the main source of EAP variability across different recordings arises from random positioning of the electrode and the morphology of the neuron—a relationship that does not provide useful information about the intracellular state of the cell. Here we show that an accurate computational model of the EAP can shed light on the source(s) of variability in recorded EAP waveforms and can contribute to the analysis of some outstanding questions in the interpretation of EAP recordings. We investigate the effects of cellular morphology, the cell's spatial dimensions, and differential expression of various ionic channels on the waveform of the EAP. We take advantage of recent developments in computational modeling to predict EAPs resulting from simulated neurons at a high level of detail (Holt 1998) and the massive increase in available computing power since the theory was developed in the 1960s (Plonsey 1969; Rall 1962). We use a unique data set (Henze et al. 2000) to reproduce the precise conditions for the generation of a set of intra- and extracellular action potentials recorded in vivo.

## METHODS

### Computational methods

The extracellular potential induced by a spike in a neuron was calculated in two distinct stages. First, we computed the transmembrane currents for a pyramidal neuron model on the basis of standard one-dimensional (1-D) cable theory (e.g., Koch and Segev 1999). Second, we used those currents to compute the extracellular potentials as described below.

**CALCULATION OF EXTRACELLULAR POTENTIALS AND THE LINE SOURCE APPROXIMATION.** It was previously demonstrated that the neuropil is well modeled by an isotropic volume conductor in which the capacitive effects of the media are negligible in the frequency range of interest to us (1–3,000 Hz). That is, we can satisfactorily describe the extracellular milieu by a purely ohmic conductivity  $\rho$  (units of  $\Omega\text{cm}$ ) (e.g., see Holt 1998; Plonsey 1969). Under these circumstances, the electric potential in the extracellular space is governed by Laplace's equation

$$\nabla^2 \Phi = 0 \quad (1)$$

where  $\Phi$  is the extracellular potential. At the boundaries,  $(1/\rho) \Phi = \mathbf{J}_m$ , where  $\mathbf{J}_m$  is the transmembrane current density and  $\rho$  is the

Address for reprint requests and other correspondence: C. Gold, Beckman Institute, 216-76, California Institute of Technology, Pasadena, CA 91125 (E-mail: carlg@caltech.edu).

The costs of publication of this article were defrayed in part by the payment of page charges. The article must therefore be hereby marked "advertisement" in accordance with 18 U.S.C. Section 1734 solely to indicate this fact.

extracellular resistivity. For a single point source of amplitude  $I$  in an unbounded isotropic volume conductor, the solution is dual to the classical physics problem of point charges in free space (Coulomb's law)

$$\Phi = \rho I / (4\pi r) \quad (2)$$

where  $I$  is a point source of current and  $r$  is the distance from the source to the measurement. Multiple current sources combine linearly by the superposition principle. In real neurons, membrane currents are distributed over elongated cylindrical processes, whose length considerably exceeds their width. The line source approximation (LSA) (Holt and Koch 1999) makes the simplification of locating the transmembrane net current for each neurite on a line down the center of the neurite. By assuming a line distribution of current, the resulting potential from Eq. 2 has a straightforward analytic two-dimensional (2-D) solution in cylindrical coordinates. For a single linear current source having length  $\Delta s$ , the resulting potential  $\Phi(r, h)$  is given by

$$\begin{aligned} \Phi(r, h) &= (\rho / 4\pi) \int_{-\Delta s}^0 I ds / \Delta s \sqrt{r^2 + (h - s)^2} \\ &= (\rho I / 4\pi \Delta s) \log \left[ \frac{\sqrt{h^2 + r^2} - h}{\sqrt{l^2 + r^2} - l} \right] \end{aligned} \quad (3)$$

where  $r$  is the radial distance from the line,  $h$  is the longitudinal distance from the end of the line, and  $l = \Delta s + h$  is the distance from the start of the line. Holt and Koch (1999) analyzed the accuracy of the LSA and found it to be highly accurate except at very close distances (i.e., about 1  $\mu\text{m}$ ) to the cable (see also Rosenfalck 1969; Tryanova and Enriquez 1991). Because extracellular recording electrodes are typically many micrometers away from neurons, we can use the LSA to calculate extracellular potentials.

The steps in the model are as follows. First, we computed transmembrane currents for a particular neuron with its complement of ionic currents (see following text) using the NEURON Simulation Environment (Hines and Carnevale 1997), assuming that the extracellular potential was constant and equal to zero. In a second step, we used the LSA to compute the extracellular potential at a select number of locations from the transmembrane currents using a custom-written Matlab program. We assumed that the previously calculated transmembrane currents would not be affected by the small changes in extracellular potential ( $\ll 1$  mV). One could refine this estimate on the basis of an iterative procedure, although this does not significantly affect the numerical results (Holt 1998).

**CALCULATION FOR INHOMOGENEOUS RESISTIVITY.** The LSA assumes an extracellular medium that is homogeneous. However, recent measurements of CA1 have found that the pyramidal cell body layer has approximately double the resistivity of the surrounding *stratum radiatum* and *stratum oriens* ( $\rho = 640, 260, 290 \Omega\text{cm}$ , respectively) (López-Aguado et al. 2001). Furthermore, these baseline resistivities may be increased by as much as 50% during periods of high activity. Because the inhomogeneity constitutes an approximately planar layer, we can use the "method of images" (Maxwell 1881; Weber 1950) to calculate its impact. Three layers of differential conductivities ( $\rho_1, \rho_2$ , and  $\rho_3$ ), separated by two parallel planes, are exactly solved by an infinite series of images with decreasing magnitudes of the form

$$I_{\text{image}} = I_{\text{original}} [(\rho_1 - \rho_2)/(\rho_1 + \rho_2)]^n [(\rho_3 - \rho_2)/(\rho_3 + \rho_2)]^m \quad (4)$$

where  $n$  and  $m$  increase for the more distant images. The magnitude of the images decline rapidly at the same time as the distance to the images increases; in practice, the infinite series is well approximated by the first few terms (results shown here use  $n, m \leq 5$ ). Including the exact calculation for the impact of the high resistivity cell body layer has only a modest impact on extracellular voltages compared with the assumption of homogeneous conductivity equal to that of the *stratum oriens* or the *stratum radiatum*. The amplitude of the extracellular action potential increases by a maximum of around 40% at the center

of the region of high resistivity, but the impact falls off rapidly with distance. Because of the modest impact on the results and the complexity of the calculation method, we defer details of the solution and our method of verification to a future publication.

### Experimental methods

Simultaneous intracellular and extracellular recordings of CA1 neurons in vivo were reported previously in Henze et al. (2000) and we briefly review the methods here. The extracellular electrodes were of three types: 1) single, 60- $\mu\text{m}$ -diameter wires, 2) "tetrodes" as described in Gray et al. (1995), or 3) silicon electrode arrays with six recording sites spaced 25  $\mu\text{m}$  apart, as described in Henze et al. (2000). During numerous attempts to obtain stable intracellular recordings from cells also recorded by the extracellular electrode, Henze et al. (2000) obtained recordings from 38 neurons: three recorded with single-wire electrodes, 22 recorded with tetrodes, and 13 recorded with silicon probe arrays.

Recordings were wideband filtered at either 1 Hz to 3 kHz or 1 Hz to 5 kHz. Averages of the EAPs were made by sampling from the extracellular recording at times triggered by the intracellular spike. In preparing averages for comparison to the model, we used only recordings from the beginning of the session until the cell started to depolarize significantly ( $>5$ –10 mV) arising from the shunt current from electrode impalement. The number of spikes available for the average range from a few hundred to a few thousand. After intracellular recordings were complete, cells were injected with biocytin and the rats were killed and their brains sliced, stained at 60  $\mu\text{m}$ , and preserved in slides. Of the 38 recorded cells, 17 cells were stained well enough for reconstruction. In these cases the complete three-dimensional (3-D) structure of recorded cells was measured using the NeuroLucida System and then used as the basis for compartmental simulations. In cases where the extracellular electrode track left some visible mark of its location (i.e., blood or debris) this was also measured and used to estimate the electrode location for comparison with the computer simulations. Visible electrode tracks were found in the CA1 area for seven cells and tracks were found in the overlying cortex only for another three cells.

We also used a larger sample of EAP recordings ( $n = 307$ ) with no coincident intracellular electrode recordings as a reference set for comparison (method as described in Csicsvari et al. 2003), to more accurately estimate the frequency of EAP features observed in the small sample of simultaneous recordings and to confirm that observed features in the simultaneous recordings were not artifacts of intracellular impalement.

### Simulation methods

Single trials of standard 1-D compartmental simulations were performed for each reconstructed cell within NEURON (Hines and Carnevale 1997) and compared with the average simultaneous intra- and extracellular recordings. The average number of compartments was around 250, based on a 3-D reconstruction that contained nearly 2,500 measurements of dendrite diameters and locations. The time steps of the simulation were varied by the CVODE method (Hines and Carnevale 2001). During the simulation, membrane currents for all compartments of the cell were saved at intervals of about 0.05–0.1 ms to calculate extracellular potentials.

**PASSIVE PARAMETERS AND SPINES.** The intracellular resistivity was set to  $R_i = 70 \Omega\text{cm}$  (Stuart and Spruston 1998). The value of this parameter had an important impact on the resulting extracellular potential amplitude. Simulations with higher values for  $R_i$  resulted in potentials that were too small to match the recording and histology data. The membrane resistance was set to  $R_m = 15 \text{ k}\Omega\text{cm}^2$  (Spruston and Johnston 1992), to account for the net effect of in vivo synaptic conductances in reducing the membrane resistance without actually

modeling the detailed time dependency of synaptic activity (Destexhe and Paré 1999). The specific capacitance was set to  $C_m = 1 \mu\text{F}/\text{cm}^2$  (Koch 1999). The reversal potential for the passive leak mechanism was set to  $V_{\text{rest}} = -65 \text{ mV}$ .

Dendritic spines are accounted for by adjusting the passive membrane parameters  $R_m$  and  $C_m$ , decreasing the former and increasing the latter by a factor  $f$  given by the normalized spine area (Major et al. 1994). Specific spine density estimates are taken from Megias et al. (2001) (for details, see APPENDIX A).

These choices resulted in average somatic input resistances of  $31.8 \pm 6.5 \text{ M}\Omega$ , which is in agreement with previous measurements of CA1 input resistances in vivo ( $48.4 \pm 11 \text{ M}\Omega$ ; Henze and Buzsáki 2001) and compatible with the notion that, because of constant synaptic bombardment in vivo, the input resistance is as much as 80% lower (Destexhe and Paré 1999) than that in vitro (Spruston and Johnston 1992).

**ACTIVE IONIC CURRENTS.** The model includes Hodgkin–Huxley style kinetic models for 12 different voltage-dependent ionic currents carried by  $\text{Na}^+$ ,  $\text{K}^+$ , and  $\text{Ca}^{2+}$  ions. The following ionic currents included in the model.

- Fast, inactivating  $\text{Na}^+$  (axonal and soma/dendritic varieties:  $I_{\text{Na}^+_{\text{Ax}}}$ ,  $I_{\text{Na}^+_{\text{SD}}}$ ) (Colbert and Pan 2002; Magee and Johnston 1995; Martina and Jonas 1997)
- A type  $\text{K}^+$  (proximal and distal varieties,  $I_{\text{K}^+_{\text{AProx}}}$ ,  $I_{\text{K}^+_{\text{ADist}}}$ ) (Hoffman et al. 1997; Klee et al. 1995)
- AHP (afterhyperpolarization) type  $\text{Ca}^{2+}$ -dependent  $\text{K}^+$  ( $I_{\text{K}^+_{\text{AHP}}}$ ) (Williamson and Alger 1990)
- C type voltage and  $\text{Ca}^{2+}$ -dependent  $\text{K}^+$  ( $I_{\text{K}^+_{\text{C}}}$ ) (Lancaster and Nicoll 1987; Yoshida et al. 1991)
- D type  $\text{K}^+$  ( $I_{\text{K}^+_{\text{D}}}$ ) (Storm 1988)
- K type  $\text{K}^+$  (also known as “DR” type,  $I_{\text{K}^+_{\text{K}}}$ ) (Klee et al. 1995)
- M type  $\text{K}^+$  ( $I_{\text{K}^+_{\text{M}}}$ ) (Halliwell and Adams 1982)
- H type mixed cation (somatic and dendritic varieties,  $I_{\text{H}_{\text{Soma}}}$ ,  $I_{\text{H}_{\text{Dend}}}$ ) (Magee 1998)
- L type  $\text{Ca}^{2+}$  ( $I_{\text{Ca}^{2+}_{\text{L}}}$ ) (Christie et al. 1995; Fisher et al. 1990; Magee and Johnston 1995)
- N type  $\text{Ca}^{2+}$  ( $I_{\text{Ca}^{2+}_{\text{N}}}$ ) (Christie et al. 1995; Fisher et al. 1990; Magee and Johnston 1995)
- R type  $\text{Ca}^{2+}$  ( $I_{\text{Ca}^{2+}_{\text{R}}}$ ) (Magee and Johnston 1995)
- T type  $\text{Ca}^{2+}$  ( $I_{\text{Ca}^{2+}_{\text{T}}}$ ) (Fisher et al. 1990; Magee and Johnston 1995)

To model these currents, we follow the style of Borg-Graham (1999). For complete details on the active ionic currents model see APPENDICES B and C.

The sodium reversal potential  $E_{\text{Na}^+}$ , was set to 70 mV.  $\text{Ca}^{2+}$  currents were modeled using a conductance-based formalism (not permeability) with  $E_{\text{Ca}} = 140 \text{ mV}$ .  $\text{Ca}^{2+}$  accumulation, diffusion, and buffering were modeled using concentric shells (APPENDIX B). We used  $E_{\text{K}} = -140 \text{ mV}$  to accurately account for perfusion of  $\text{K}^+$  from the intracellular electrode. This is based on using the Nernst equation where the extracellular concentration of  $\text{K}^+$  is 5 mM. Normally, the intracellular  $\text{K}^+$  concentration is 140 mM. However, the sharp pipette contains 1 M  $\text{K}^+$  and, given the fact that larger molecules like biocytin effectively perfuse from a pipette during current injection (which was applied throughout recording), the soma and apical shaft will most likely approach this level. Although the concentration will be close to 140 mM in oblique and distal dendrites as a result of active membrane processes restoring the  $\text{K}^+$  balance, it is the soma and apical shaft that make the largest contribution to the generation of observable EAPs. Consequently, we simplify the model by assuming a constant 1 M intracellular  $\text{K}^+$  concentration. Our experiences tuning the model, as described in RESULTS, led us to the conclusion that any

inaccuracies resulting from this assumption are small compared with those of other sources of uncertainty in the biophysical parameters; the most likely consequence is slightly different tuned active current conductance densities compared with a model incorporating details of  $\text{K}^+$  perfusion and active  $\text{K}^+$  membrane pumps.

The exact kinetics and densities of the currents were tuned to match the simultaneous intra- and extracellular recordings taken in vivo while remaining faithful to the qualitative properties that were established by in vitro studies. This includes the nonuniform distribution of active ionic current conductances (as detailed in APPENDIX C). In general, the time constants were found to require values significantly faster than those measured in vitro and, when necessary, activation/inactivation curves were modified as well. The peak conductance densities associated with each current were treated as variables that needed to be tuned to match the simultaneous intracellular and extracellular recording, leaving the passive parameters and active ionic current kinetics fixed for all cells. The parameters tuned are those listed in Tables C1, C2, and C3 (see APPENDIX C).

**MODEL AXON.** The axon for each cell was modeled with a structure similar to that described in Mainen et al. (1995): the diameter of the axon is 1/20th the diameter of a sphere having the same surface area as that of the measured soma. An axon hillock 10  $\mu\text{m}$  long connects the soma to the initial segment, beginning at  $4 \times$  the axon diameter and tapering to the axonal diameter. The initial segment is 15 microns long. After the initial segment the axon for pyramidal cells consists of alternating myelinated sections (100  $\mu\text{m}$  long) and nodes of Ranvier (1  $\mu\text{m}$  long).

Although Mainen et al. (1995) used a very high density of  $\text{Na}^+$  currents to cause axonal action potential initiation ( $1,000 \times$  the somatic density), we used a model similar to that suggested by Colbert and Pan (2002): the initial segment and nodes of Ranvier have a  $\text{Na}^+$  current conductance density that is only moderately higher than the soma ( $1\text{--}3 \times$ ) but the  $\text{Na}^+$  current in the initial segment and nodes of Ranvier ( $I_{\text{Na}^+_{\text{Ax}}}$ ) has kinetics that activates at less depolarized potentials than the  $\text{Na}^+$  current in the soma and dendrites ( $I_{\text{Na}^+_{\text{SD}}}$ ). This usually resulted in an action potential that initiates at the first node of Ranvier 0.5–1 ms before spreading to the soma by the initial segment and then to the dendrites. However, as described in *Result of dendritic initiation* (Fig. 7), our experiments suggest that there can be variability in the pattern of initiation with interesting consequences. For details on the kinetics and density for  $\text{Na}^+$  currents see APPENDICES B and C.

**ELECTRODE SHUNT AND DRIVING INPUTS.** The cell was stimulated by a relatively low amplitude tonic current injection,  $<1 \text{ nA}$  (Henze et al. 2000). An electrode shunt,  $R_{\text{shunt}}$  between 50 and 200  $\text{M}\Omega$ , modeled the impact of the sharp electrode on the cell. The shunt was located at either the soma or in an apical trunk compartment in cases where the height of the action potential and lack of pronounced AHP in the intracellular recording suggested it was distal from the soma (Kamondi et al. 1998).

Synaptic input was mimicked by varying the leak resistance and reversal potential for the more distal compartments assumed to be receiving synaptic input. Typically, this meant reducing  $R_m$  by a factor of 3 to 5, and applying a reversal potential to the leak current of between  $-55$  and  $-30 \text{ mV}$  to mimic a mixed excitatory and inhibitory synaptic input.

### Performance

Simulations were 25 ms long: the first 10 ms were used to establish the stability of the rest potential (between  $-70$  and  $-60 \text{ mV}$ ) given by the combination of active currents without synaptic input. Simulated synaptic input was switched on to depolarize the cell, from 1 to 5 ms, until an action potential was triggered and the cell repolarized and returned to a stable rest potential as judged by remaining stable for the final 10 ms of the simulation. In addition a 4-ms extracellular spike



trace at 10 locations was computed. All the above took 1–2 min, long enough that a brute-force automatic search for optimal parameters to match the simulations to the recordings was not feasible. Consequently, the primary method for tuning the channel density parameters of the model consisted of manual trials, supplemented by an automated local search of the parameter space (see *Estimation of simulated EAP accuracy* below).

## RESULTS

### Membrane currents and the extracellular potential waveform

The simultaneous intra- and extracellular recording along with the model simulation matching the recording for cell D151 is shown in Fig. 1. As can be seen by comparing the total membrane current ( $I_{\text{total}}$ ) to the EAP, the shape of the waveform is proportional to the time profile of  $I_{\text{total}}$  across the membrane of the perisomatic compartments. This is a straightforward consequence of the basic equation of the extracellular potential (Eq. 2) and the superposition principle. Note that, although the apical trunk compartment in the figure has a net current peak amplitude approximately 1/5 to 1/10 that of the soma, there are several other proximal dendritic compartments with virtually identical current versus time profiles. This gives the proximal dendrites about equal weight to the soma in determining the shape of the waveform. An additional consequence of Eq. 2, that will be further analyzed below, is that

distal dendritic compartments make virtually no contribution to the EAP in the perisomatic region (i.e., the waveform detectable by an extracellular recording electrode). This is because the smaller diameter of the individual distal dendrites results in smaller net currents and the greater distance further reduces the impact.

### Electrode position and the capacitive phase of the EAP

Another example of an EAP is illustrated in cell D068 (Fig. 2). As in most recordings, the EAP lacks a prominent capacitive current phase. The capacitive phase peak for cell D151 (Fig. 1) is 9% of the amplitude of the  $\text{Na}^+$  phase peak; in all 38 recordings in Henze et al. (2000) only four have a capacitive phase peak that is comparable or larger. We compared these results to the sample of 307 EAPs recorded without a simultaneous intracellular recording and found that 73% of the waveforms had a capacitive peak that was <5% of the amplitude of the  $\text{Na}^+$  peak, whereas 95% of the recordings had a capacitive peak amplitude that was <10% of the amplitude of the  $\text{Na}^+$  peak. The overall average ratio was 6%, and the distribution had a long tail, including a handful of recordings for which the ratio of the capacitive phase peak to the  $\text{Na}^+$  peak was close to 100% (recordings from Henze et al. 2000 contained two such waveforms).

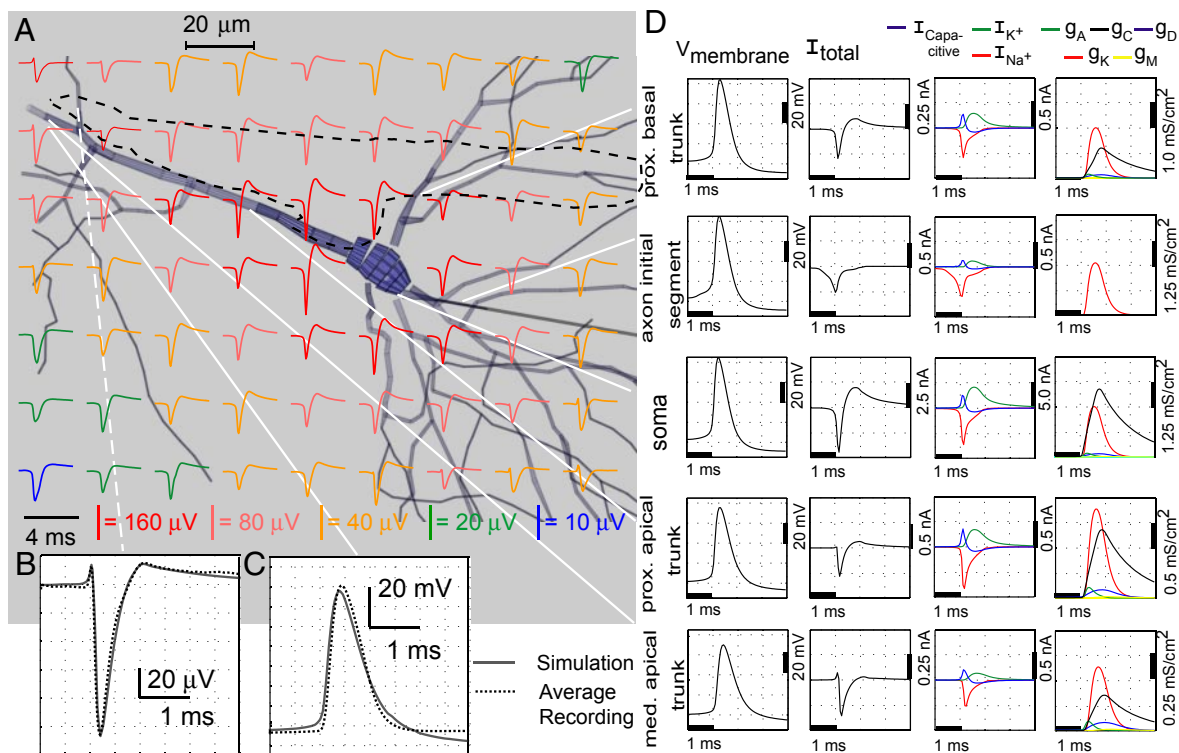


FIG. 1. Recording and Simulation D151. *A*: extracellular action potentials (EAPs) in the transverse section containing the soma and the tip of the electrode track (dotted line). *B*: enlargement of the EAP at the estimated electrode position, and comparison to the recording (strongest channel of the tetrode). EAP is made up of 3 distinct phases: 1) a brief, positive peak; 2) a much larger negative peak; and 3) a positive period of longer duration and slowly decaying amplitude. *C*: comparison of the average intracellular recording with the simulated spike in the proximal apical trunk. Lack of pronounced afterhyperpolarization (AHP) suggests the intracellular electrode was not at the soma. *D*: details of the simulation in the indicated compartments. Shape of the EAP waveform is given by the shape of the net membrane current across the membrane at the soma and proximal dendrites (2nd column). Third column: makeup of the membrane current in terms of  $\text{Na}^+$ ,  $\text{K}^+$ , and mixed-ion capacitive current. All 3 currents are simultaneously active throughout the action potential (AP); the 3 phases of the EAP correspond to the current that is dominant at that time: Brief positive peak at the start of the waveform is attributed to the positive capacitive current; the main negative peak is attributed to the influx of  $\text{Na}^+$  current driving the action potential; the final positive phase results from repolarizing  $\text{K}^+$  current flowing out of the cell. Last column: corresponding conductivity densities of the A, C, D, K, and M type  $\text{K}^+$  currents.

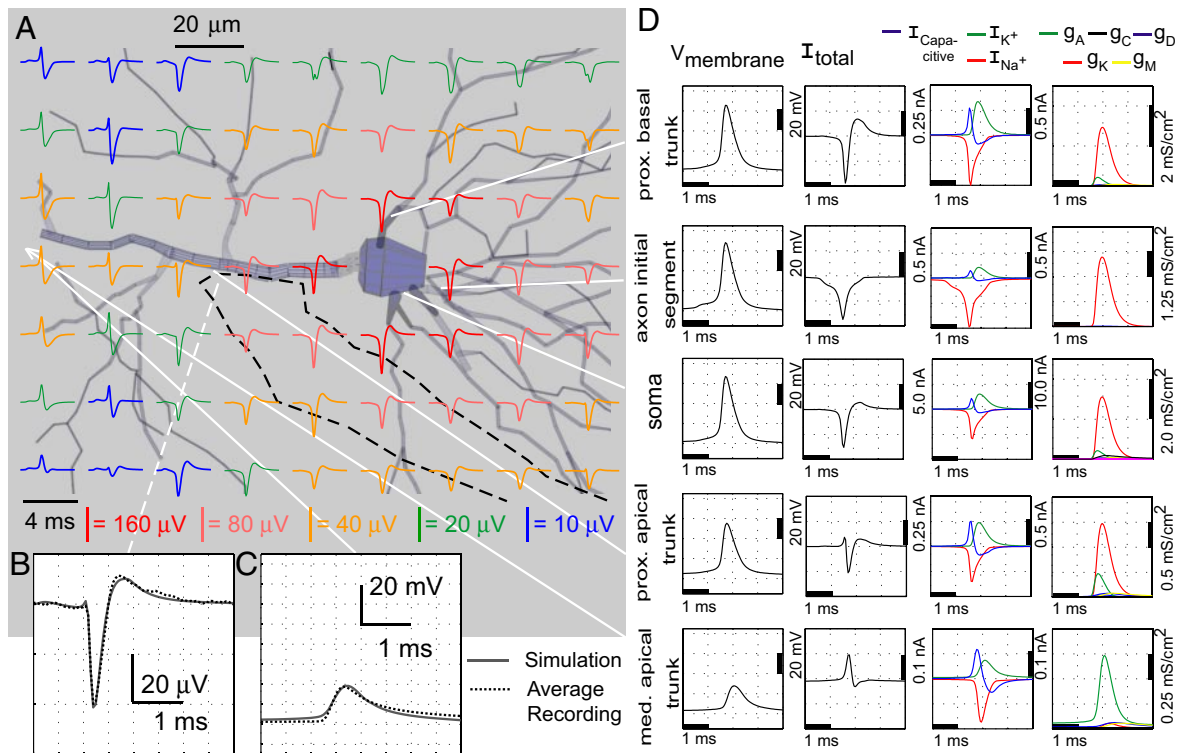


FIG. 2. Recording and Simulation D068. **A:** EAPs in the transverse section containing the tip of electrode track (dotted line), about  $5\ \mu\text{m}$  caudal to the soma and apical trunk (the  $z$ -axis is the axis perpendicular to the plane of the section). Close to the soma, there is no initial, positive peak in the EAP. At locations along the apical trunk, the initial peak becomes pronounced. **B:** comparison of extracellular recording (strongest channel of the tetrode) and simulation at the estimated electrode position. There is only a slight hint of a positive deflection before the negative  $\text{Na}^+$ -dominant phase of the waveform. **C:** comparison of intracellular recording and the simulation in the apical trunk approximately  $120\ \mu\text{m}$  from the soma. **D:** further simulation details. In the soma (middle row) the positive capacitive current, proportional to the change in membrane potential, coincides with the larger  $\text{Na}^+$  current (3rd column) because the membrane potential change is driven by local  $\text{Na}^+$  current. In dendritic compartments (4th and 5th rows) the membrane depolarization is initially driven by  $\text{Na}^+$  current from the soma, until local  $\text{Na}^+$  currents are activated and the action potential regenerates. In the brief time before the local  $\text{Na}^+$  currents activate, the positive capacitive current is the dominant membrane current and a capacitive-dominant phase is visible in the net current (2nd column). Consequently, the EAP has a more pronounced capacitive phase close to the apical trunk. Also shown, the  $\text{Na}^+$  current starts to enter the axon initial segment (2nd row) in a gradual way, driven by the action potential in the first node of Ranvier (not shown) and before the start of the main action potential at the soma. This results in a slightly negative slope in the extracellular potential before the start of the main EAP.

The reason that the majority of the recordings exhibit little or no capacitive current in the EAP is demonstrated in Fig. 2. During a typical action potential initiation the membrane potential change at the soma is driven by local  $\text{Na}^+$  current, and thus there is no significant capacitive current until after the  $\text{Na}^+$  current is already active. Because the inward  $\text{Na}^+$  current is of greater amplitude than the outward capacitive current, the total current lacks an initial positive peak. In contrast, in the more distant dendrites there is a brief interval between the initial, passive, depolarization, and the active regeneration of the action potential through local  $\text{Na}^+$  channel openings. Also, the  $\text{Na}^+$  conductance density is typically lower in the dendrite than at the soma (arising from slow inactivation, as described in APPENDIX C) and, consequently, the capacitive current is relatively larger. As a result of these factors, at the start of the action potential (AP), the positive capacitive current is the largest membrane current and a positive capacitive-dominant phase is present in the total current. This explains the previously observed phenomenon that an initial, positive, capacitive phase is usually visible in EAP waveforms recorded from CA1 pyramidal cells when the tip of the recording electrode is situated along the apical trunk at some distance from the soma (Buzsáki and Kandel 1998). Simulations suggest that waveforms with a capacitive phase of the same size as the  $\text{Na}^+$

phase may result from a distal dendritic AP initiation that then propagates forward to the soma: the reversal of the initiation process described above leads to the disappearance of the capacitive phase of the EAP in the distal apical region and the appearance of an enlarged capacitive phase around the soma and the basal dendrites.

Cell D068 (Fig. 2) also illustrates the contribution of the axon to the EAP: because of the lower threshold of activation, the axon initial segment  $\text{Na}^+$  current activates before the soma  $\text{Na}^+$  current. This creates a slight depolarization at about  $0.5\ \text{ms}$  before the start of the more prominent three-phase EAP described above. However, most of the  $\text{Na}^+$  current in the initial segment is coincident with the somatic  $\text{Na}^+$  current and adds to the amplitude of the EAP peak. Although the AP typically initiates at the first node of Ranvier nearly  $0.5\ \text{ms}$  before the AP spreads to the soma, the myelinated axon and nodes of Ranvier make no contribution to the EAP. The myelinated axon lacks active channels and has only passive and capacitive currents that are very small relative to the active perisomatic currents. The nodes of Ranvier are too small and isolated to significantly contribute to the amplitude of the EAP: the peak  $\text{Na}^+$  current in the node is typically about  $0.05\ \text{nA}$ , two orders of magnitude less than the peak  $\text{Na}^+$  current in the soma.

Although the model does predict significant variation in the shape of the EAP waveform at distal locations, practically all of the significant variability occurs at amplitudes below the threshold of detectability. In Figs. 1–3 only the *red* and *pink* traces are above the typical detection and sorting threshold, about 60  $\mu\text{V}$ , in CA1 (Henze et al. 2000). Aside from the aforementioned increase in the capacitive phase of the waveform along the apical trunk, in the region around the soma where an extracellular electrode would detect the spike above the background noise there is relatively little variation in the shape of the waveform, only an increase in amplitude as the electrode is moved closer to the soma.

#### Active current conductance density and the EAP waveform

The recording of cell D112.1 (Fig. 3) illustrates two other sources of variability seen in average EAPs of CA1 pyramidal cells: the width of the  $\text{Na}^+$ -dominant phase may vary and show inflection points in the transition to the  $\text{K}^+$ -dominant phase, and also the amplitude and shape of the  $\text{K}^+$ -dominant phase may vary. The model suggests that this variability reflects differences in the conductance densities of active ionic currents, rather than electrode position.

Figure 3 illustrates how the width of the  $\text{Na}^+$ -dominant phase of the EAP is influenced by the timing of the  $\text{K}^+$  currents. Variability in the timing of the net  $\text{K}^+$  current can occur because there are at least five different  $\text{K}^+$  currents

(types A, C, D, K, and M) that make a contribution to the repolarization of the action potential and each type has unique properties with respect to the onset time and duration of the  $\text{K}^+$  current it generates. The A current is fast and inactivating; the C current is slower to activate and also inactivates slowly as a result of  $\text{Ca}^{2+}$  dependency; the D current is slow but has a low threshold of activation, being active at rest; the K current is fast but has a relatively high activation threshold; and the M current is the slowest but has a low threshold of activation, although not low enough to be active at rest. Although the C and K currents tend to dominate repolarization at the soma, the M and A currents make a larger contribution in the distal dendrites where the C current is not present (as described in APPENDIX C) and where the AP amplitude is too low to trigger significant K current.

Reproducing the simultaneous intra- and extracellular recordings with the model led us to the conclusion that it was necessary to assume significant variation in the conductance density levels of the  $\text{K}^+$  currents to achieve reasonable matches between recording and simulation. This was particularly the case when trying to match the width of the  $\text{Na}^+$  phase and the shape of the  $\text{K}^+$  phase in the extracellular waveform. Evidence for varying levels of expression of ionic channels in pyramidal cells has been found in the analysis of gene expression profiles (Toledo-Rodriguez et al. 2004). The peak conductance densities used to match the waveforms are given in

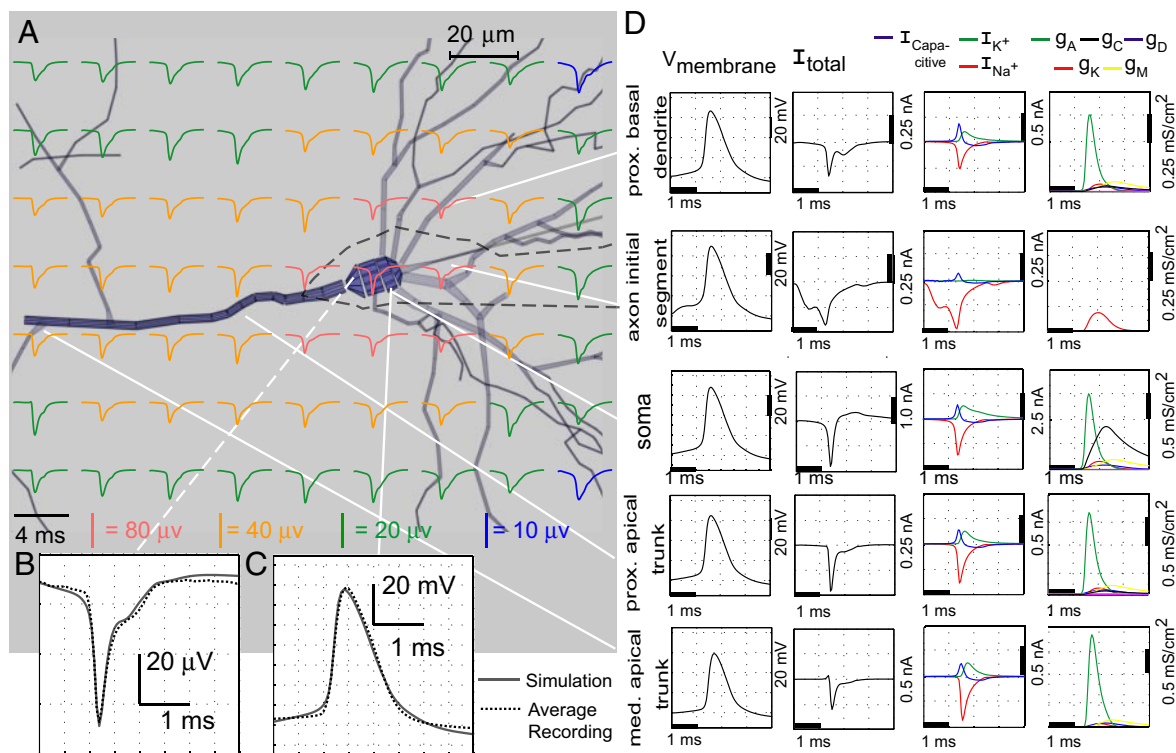


FIG. 3. Recording and Simulation D112.1. *A*: EAPs in the transverse section containing the electrode track (dotted line), about 25  $\mu\text{m}$  caudal to the soma and apical trunk (the  $z$ -axis is the axis perpendicular to the plane of the section). *B*: enlargement of the EAP at the estimated electrode position, and comparison to the recording (strongest channel of the tetraode). An initial positive peak is completely absent, and the  $\text{Na}^+$ -dominant negative phase is made up of a narrow peak followed by a period of slower repolarization.  $\text{K}^+$ -dominant phase is of minimal amplitude. *C*: comparison of intracellular recording and simulation at the soma. *D*: selected details of the simulation. Duration of significant  $\text{Na}^+$  channel activation is longer than the  $\text{Na}^+$ -dominant phase seen in the EAP. Width of the  $\text{Na}^+$ -dominant phase in the EAP is therefore determined by the timing of the  $\text{K}^+$  currents: strong A and C type currents (rightmost column). Very fast A current shapes the sharp peak of the  $\text{Na}^+$  phase by quickly counteracting  $\text{Na}^+$  current, although the A current rapidly inactivates. C current continues the repolarization in the somatic compartment, but has a much lower density in the dendritic compartments. This leads to the widening of the  $\text{Na}^+$  phase and the negligible amplitude of the  $\text{K}^+$  phase. Shape of the EAP (*B*) is similar to the current profile of the proximal dendrites (1st, 4th, and 5th rows, 2nd column).



Tables C1, C2, and C3 in APPENDIX C. Although the variability in the peak  $\text{Na}^+$  conductance density (as measured by a single SD) is on the order of only 25% of the mean, for the primary  $\text{K}^+$  currents the variability is of the same order of magnitude as the average.

For the model to match the narrow  $\text{Na}^+$ -dominant phase (0.35 ms, measured as the width at 25% of peak amplitude) and rapidly decaying  $\text{K}^+$  phase in the EAP of cell D068 (Fig. 2) requires a dominant K type  $\text{K}^+$  current to rapidly counteract the  $\text{Na}^+$  current and achieve repolarization. Cell D151 (Fig. 1) has a somewhat longer-duration  $\text{Na}^+$  phase and a  $\text{K}^+$  phase that decays more slowly, and the best match with the model is achieved by assuming a balanced combination of C and K type  $\text{K}^+$  currents. Cell D112.1 (Fig. 3) is relatively unusual in that it has a sharply peaked  $\text{Na}^+$  phase in which the transition to the  $\text{K}^+$  phase slows significantly midway, leading to a relatively long duration  $\text{Na}^+$  phase that lasts 0.95 ms. Only three of 38 of the waveforms (Henze et al. 2000) had a similar shape and in a larger sample of EAP recordings (with no associated intracellular recording); the proportion having such a waveform was similar (27 of 307). This type of waveform was best matched by a repolarization consisting of primarily A and C type currents.

Although the amplitude of the waveform varies (generally getting smaller as a recording session progresses), there is little change in the waveform of the EAP during recording sessions that last up to 2 h. This suggests that the conductance density differences between cells are stable on this timescale.

#### Estimation of simulated EAP accuracy

The quality of fit values between the simulation and recording achieved by these methods are listed in Table 1. The measure of error used is the square root of the mean square

error (SMSE) between the recording and the simulation. The SMSE is then normalized by the peak amplitude to enable comparison of the error on intra- versus extracellular recordings and on cells with EAPs of different amplitude. For comparison of the model with the extracellular recording, we also weighted the mean square error to emphasize an accurate match for the samples at the peak amplitude: the sample for the negative ( $\text{Na}^+$ ) peak was weighted  $10 \times$  that of a nonpeak sample, the points immediately before and after the peak were weighted  $5 \times$ , and the points two samples distant from the peak were weighted  $2.5 \times$  (weights on all sample points were then normalized). Because of the longer duration of the intracellular action potential (IAP) peak, weighting was not necessary to ensure that the SMSE reflected a close match to the peak amplitude. For single-wire and tetrode recordings, we compare the simulated EAP with the largest-amplitude channel. For silicon probe recordings, we calculate the SMSE for all channels with peak amplitudes  $>20 \mu\text{V}$  and report the average.

The comparison between model and recording was made at the best spatial estimate of the electrode location whenever possible, or at a plausible location if there was no visible electrode track. In all cases where the electrode location could be estimated, the model produced a good estimate of the amplitude of the EAP at that location. Unfortunately, because of their low profile, none of the silicon probe recordings produced a visible electrode track in the CA1 area. Nevertheless, the model produced a good match to the sequence of EAP amplitudes on the different recording sites at plausible electrode positions (i.e., nearly parallel with the apical trunk), coming within a reasonable distance of the soma as suggested by the maximum-amplitude recording (Fig. 7).

The method used to tune the conductance densities of the active ionic current was a combination of manual tuning and

TABLE 1. Measure of error between the recordings and simulations

Cell	Recording Simulation						No. of Sites >20 $\mu\text{V}^*$
	Intracellular			Extracellular			
	Amplitude, mV	$\sqrt{\text{MSE}}$ , mV	% Error	Amplitude, $\mu\text{V}$	$\sqrt{\text{MSE}}$ , $\mu\text{V}$	% Error	
D037	52.7	2.3	4.4	15.6	1.9	12.2	NA
D056	48.3	1.7	3.5	95.1	5.8	6.1	NA
D068	17.5	1.6	9.1	41.0	1.6	3.9	NA
D128	60.9	3.7	6.1	30.3	1.5	4.9	NA
D081	65.5	1.9	2.9	66.7	2.2	3.3	NA
D112.1	28.9	1.9	6.4	64.4	4.7	7.3	NA
D112.2	55.8	2.9	5.2	40.0	2.8	7.0	NA
D135	50.5	1.6	3.2	21.9	0.9	4.3	NA
D137	70.8	3.6	5.1	4.7	0.7	15.0	NA
D145	79.5	2.1	2.7	110.0	4.4	4.0	NA
D147	42.0	1.6	4.3	21.7	1.7	7.7	NA
D149	57.3	4.8	8.4	10.9	1.8	16.5	NA
D151	72.7	4.3	5.9	109.1	3.6	3.3	NA
D163	75.6	2.6	3.5	64.0	5.7	8.9	3
D180	72.1	3.0	4.2	36.6	3.4	9.3	4
D187	53.1	4.1	7.7	58.6	8.9	15.2	5
D188	78.5	4.2	5.4	48.3	19.0	39.3	3
D189	35.8	3.7	10.4	35.6	2.9	8.0	2
Average	56.5	2.9	5.5	48.6	4.1	9.8	NA
SD	17.6	1.1	2.2	31.8	4.3	8.5	NA

Square root of the mean square error (SMSE) at the recording sample points over a 4-ms window beginning 1 ms before the peak of the AP. The SMSE is normalized by the height of the intracellular AP and by the amplitude of the extracellular peak, respectively, to obtain percentage error. \*For silicon probe recordings (D163–D189), the number of sites used in calculating the SMSE and % Error, as described in *Estimation of simulated EAP accuracy* (in RESULTS).

automated search. Manual tuning of the parameters was directed by three principles: 1) the net  $\text{Na}^+$  current for the perisomatic region must produce the observed peak amplitude in the intracellular and extracellular APs; 2)  $\text{K}^+$  conductance densities in the perisomatic region are tuned to match the shape of the  $\text{K}^+$ -dominant phase of the EAP waveform; 3) distal  $\text{K}^+$  currents are tuned so that the IAP in the simulation repolarizes at the rate given by the intracellular recording. The flow of significant axial currents in the cell (an order of magnitude greater than the membrane current in a typical dendritic compartment) means that M and A type  $\text{K}^+$  currents in the distal dendrites can result in significant repolarization to the soma and proximal dendrites while having virtually no contribution to the routinely recorded EAP.

After a reasonably good fit was achieved by manual exploration of the parameter space (i.e., normalized SMSE close to 5% for a recording with amplitude  $>20 \mu\text{V}$ ), an additional local search in the parameter space was performed using the Nelder–Mead simplex algorithm. Improvements to the match were relatively modest, typically  $<1\%$  SMSE for both the intracellular and extracellular waveforms. The parameter values tested by the search were typically within a few percent of the values at the initial starting point. When we attempted to tune the conductance density parameters solely with the automated search (starting from average values for the parameters) the resulting error was invariably inferior to that achieved by manual tuning. This suggests that the performance landscape in the parameter space is nonconvex, with many local optima.

Despite this obstacle and the high degree of variability in our data, we succeeded to model both intra- and extracellular data to within 10%. This could be achieved because the degree of nonconvexity arising from parameter variations at a fine scale is less significant than the relatively constrained choices available for a few dominant parameters. For a given recording, the choice of  $\text{Na}^+$  conductance density is well constrained by the requirement that the net  $\text{Na}^+$  current reproduces the peak amplitude of both the intra- and extracellular APs. Only the precise balance between somatic and dendritic densities leads to local optima in performance. At the same time, the choice of the dominant  $\text{K}^+$  conductance is constrained by the shape of the EAP: in all cases we examined cells whose  $\text{K}^+$  phase begins and ends rapidly were best matched by a dominant K type conductance, whereas cells with a  $\text{K}^+$  phase that begins and ends more slowly were best matched by a dominant C type conductance. Given that the timing of onset and offset, activation threshold, and density distributions of the  $\text{K}^+$  conductances are fixed to be consistent with *in vitro* studies (as described in APPENDIXES B and C) the model results suggest that the choice for which  $\text{K}^+$  conductance(s) dominate in a given cell are well constrained: it is fine-tuning the exact trade-off between the  $\text{K}^+$  currents that are less significant that creates many local optima. These observations lead us to conclude that the tuned parameters for conductance densities do, in fact, represent relatively unique combinations of dominant current types. Better results from the automated search may result from methods designed to escape from very small local optima, such as simulated annealing.

Although it is possible to match simultaneous intra- and extracellular recordings with a compartmental simulation, it is actually exceedingly difficult to simultaneously achieve low errors on both. Interestingly, we find that matching the EAP

seems to be a tighter constraint on the model parameters than matching the IAP. Table 1 shows that lower errors were achieved for the match to the intracellular recording than the extracellular recording in nearly every case, despite equal weight being assigned to both errors in the manual and automated parameter tuning: the average error for all intracellular recordings is 5.5%, whereas the average error for all extracellular recordings is 9.8%. Figure 4 illustrates this point further by demonstrating that a model cell can have virtually identical membrane potentials despite significant changes in the distribution of active current densities. The extracellular waveform varies to a much greater degree when the distribution of active currents is changed. Consequently, it would be very unlikely to have significant changes in the IAP (peak amplitude, duration, or magnitude of AHP) attributed to conductance density changes without having a significant impact on the EAP. This results from the fact that the membrane potential in any given compartment combines membrane currents with axial currents, whereas the EAP results directly from the active membrane currents in the perisomatic region alone. This gives the membrane potential additional degrees of freedom compared with the extracellular potential.

#### Electrode position and width of $\text{Na}^+$ phase

Earlier we presented evidence that the main impact of electrode position (other than on the amplitude of the EAP) was on the presence or absence of a positive capacitive-dominant peak in the waveform, and that the main determinant of the width of the  $\text{Na}^+$ -dominant phase is the balance of ionic currents. However, the position of the extracellular electrode makes a secondary contribution to the duration of the  $\text{Na}^+$ -dominant phase of the waveform, as shown in Fig. 5: the more

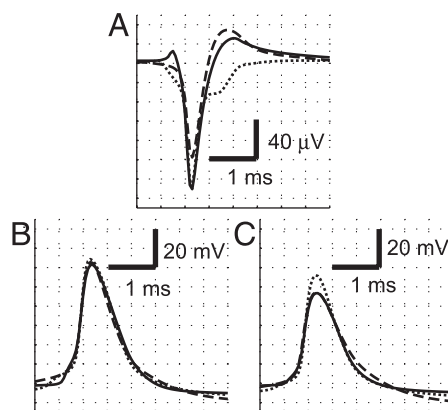


FIG. 4. A: an EAP at  $(x = -20, y = 20, z = 0)$  for cell D151 simulated with 3 different distributions of active currents. EAP changes significantly as a result of the change in parameters: the EAPs each have normalized error [square root of the mean square error (SMSE)] of about 12.5% with each other. B: intracellular membrane potentials at the soma for the same simulations. Parameters have been tuned so that the membrane potentials are virtually identical, despite the very different EAPs: average SMSE is 3.5%. C: intracellular membrane potentials in the apical trunk at a distance of nearly 100 microns from the soma: the average SMSE is 5.5%. Although at this location the membrane potential reflects the difference in the active current conductance densities more than at the soma, the introduction of a second membrane potential measurement as a constraint does not provide as much of a measure of error as a single EAP measurement. Because of the high dependency of the EAP on the precise active current conductance density the reverse result—similar EAPs for different intracellular membrane potentials—would be exceedingly unlikely.



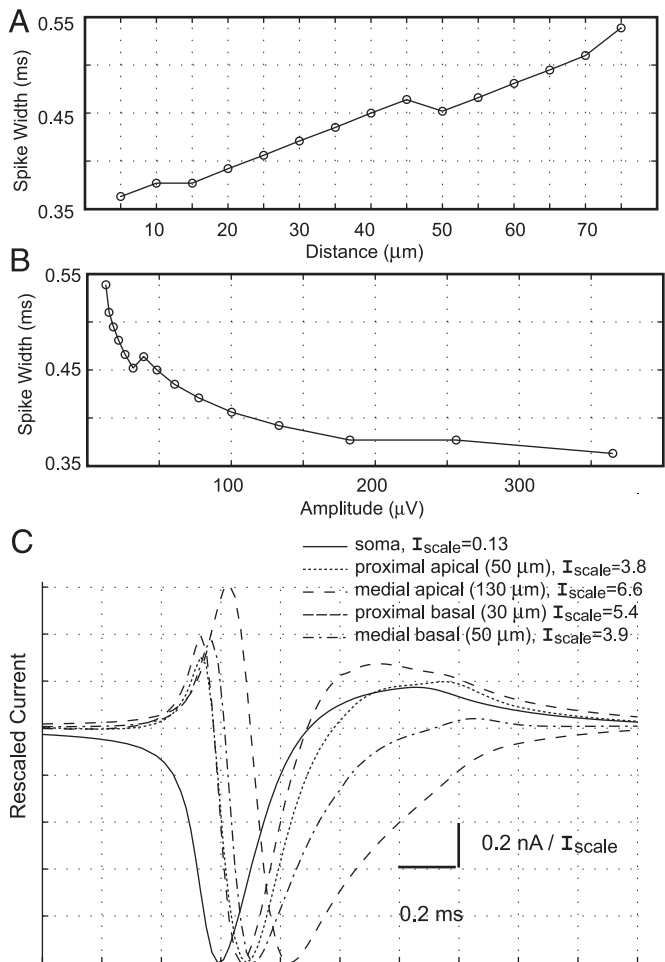


FIG. 5. *A*: duration of EAP  $\text{Na}^+$  phase vs. the simulated electrode position when moving away from the soma in a direction perpendicular to the apical trunk. Duration is measured as the width at 25% peak amplitude of the  $\text{Na}^+$ -dominant (negative) phase. There is a nearly linear relationship between the duration of the  $\text{Na}^+$ -dominant phase and the distance from the electrode to the soma. *B*: same data as in *A*, plotted vs. the amplitude of the waveform. *C*: membrane current vs. time at different locations illustrates the time required for the action potential to propagate back into the dendrite. Combined inward current phase of the soma and proximal dendrites makes a reasonably close prediction for the apparent duration of the  $\text{Na}^+$  phase observed at 45  $\mu\text{m}$ , around 0.4 ms.

distant the electrode from the cell, the longer the duration of the  $\text{Na}^+$ -dominant phase. It follows that the duration of the  $\text{Na}^+$  phase of the EAP should be negatively correlated to the amplitude of the EAP. This relationship was analyzed in the sample of 307 EAP recordings made by silicon probes. The resulting correlation coefficient between the duration of the  $\text{Na}^+$  phase (as measured as the width at 25% peak amplitude) and the amplitude was  $-0.246$  ( $P = 1.4 \times 10^{-5}$ ).

The phenomenon occurs because action potentials take time to backpropagate and because voltage amplitudes decay with distance from the current source (as in Eq. 2). A recording electrode close to the soma will effectively “see” only the somatic and most proximal dendritic current sources. This is not only because of the larger currents, but also because any contribution from a distal source will be scaled by a much greater distance. If the electrode is moved away from the cell, however, it effectively sees both the currents from the somatic initiation of the action potential and also the backpropagation

of the action potential into the dendrites because they will have similar scaling as a result of distance. Because the backpropagation along the main dendrites takes a significant fraction of a millisecond, to a distant recording electrode it looks like the extracellular potential results from a single static current source of longer duration when in fact it is produced by multiple moving current sources of short duration.

### Cell morphology

A salient aspect of the reconstruction and simulations that had very little impact on the EAP waveform was the details of each cell’s dendritic morphology. To demonstrate this relative indifference, we performed simulations using the reconstructed morphology of a CA1 basket cell (Gulyas et al. 1999) with the membrane parameters tuned to match one of our recordings from a pyramidal cell (Fig. 6). Although a pyramidal cell has a single apical dendrite and a skirt of basal dendrites extending from opposite ends of a conical soma, this basket cell has an approximately spherical soma with two thick dendrites and an assortment of narrow dendrites extending at more irregular angles. However, the resulting EAP very closely matches the original recording. We also observe that given the freedom to choose the electrode distance from the soma (to match the amplitude of the waveform), we can match virtually any EAP waveform using an arbitrarily chosen CA1 pyramidal cell for the simulation. This results from the fact that the observable waveform is determined by the net current profiles of the perisomatic compartments: if the distribution of active currents in the perisomatic region is similar for two cells, then the EAP waveform will be similar regardless of the precise location and branching pattern of the dendrites. These observations suggest that the major determinant of the EAP waveform depends primarily on the unique distribution of active current densities and considerably less on the morphological details of the cell.

At the same time, we found that the size of the neuron from each recording session was strongly correlated with the amplitude of the resulting EAPs. For example, we compared the

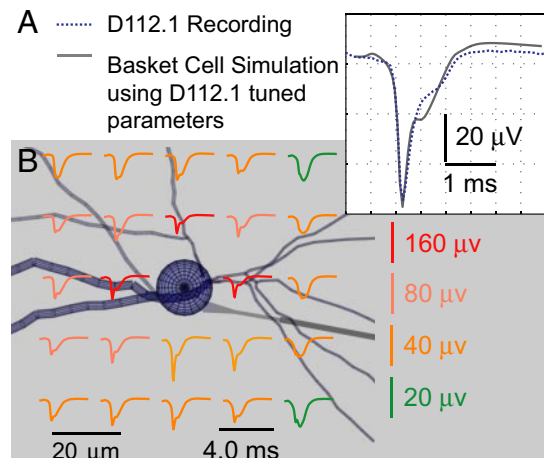


FIG. 6. CA1 Basket cell PV08D (Gulyas et al. 1999) simulated with the conductance densities tuned to match the recording for the pyramidal cell D112.1 (Fig. 3). *A*: extracellular waveform is virtually the same as that for neuron D112.1, which suggests that the dendritic morphology makes little direct contribution to the waveform. *B*: EAPs around the simulated basket cell in the plane of the soma. EAPs below threshold are somewhat different from those for D112.1, but the above threshold EAPs are very similar.

peak amplitude predicted by the simulations at a reference position 20  $\mu\text{m}$  from the soma when all the cells were simulated with identical active current conductance densities (the average values shown in Tables C1–C3). We found that amplitude ranged from 48  $\mu\text{V}$  for the smallest cell up to 164  $\mu\text{V}$  for the largest (cell size measured by the soma surface area), whereas the correlation coefficient between amplitude and cell size was 0.82 ( $P = 3.1 \times 10^{-5}$ ). However, there are multiple factors contributing to the peak amplitude of the EAP (such as  $\text{Na}^+$  current density, the assumptions regarding the resistivity, etc.), which will be the subject of a detailed analysis in a future publication.

### Result of dendritic initiation

As mentioned earlier, the model predicts a variety of EAP waveforms in the subthreshold region of the basal dendrites, as in Fig. 7. Note that the pyramidal cell recorded in the session was not stained sufficiently for reconstruction, and so simulations were performed with a cell reconstructed from another session. As the simulation demonstrates, a “W”-shaped waveform can result from an AP in a single cell and does not require coincident firing in two nearby cells. The EAP is produced by

superposition of the waveform resulting from an AP that initiates in a single dendrite and then propagates to the soma and then to a second dendrite close to the recording site. (The AP in the axon initiates before the soma but slightly after the first dendrite.) The two negative peaks in the waveform occur from two distinct  $\text{Na}^+$  influxes into two dendrites near the recording site. The dendritic initiation arises from a combination of strong synaptic input in the basal dendrite, below average  $\text{Na}^+$  density in the axon (but still greater than that in the soma), and a single dendrite having higher input resistance, as a result of smaller size, relative to the other dendrites. The amplitude of the  $\text{Na}^+$  phase peak in the “W” waveform is  $<10 \mu\text{V}$  and, although they appear clearly in an average of several hundred spikes, such waveforms would not be detected if it were not for the fact that the six-site probe also had recording sites close to the soma. Five of 13 silicon probe recordings from Henze et al. (2000) revealed similar waveforms on distal recording sites. Recordings and modeling experiments prove that a large variety of waveforms can occur depending on the exact proximity to the local basal dendrite(s) and the exact pattern of initiation. In rare cases “W” waveforms occur at high amplitude. One recording in the data from Henze et al. (2000) was of a large-amplitude (about 40  $\mu\text{V}$  negative peak ampli-

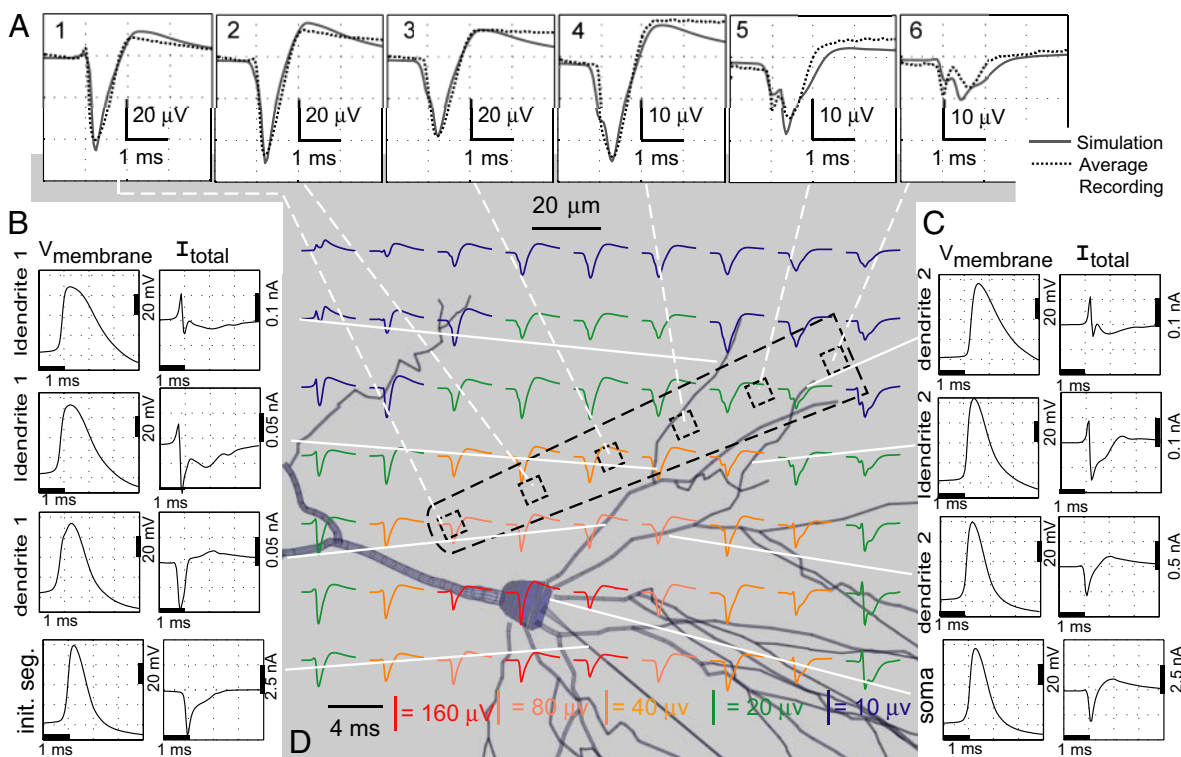


FIG. 7. A: extracellular recording and simulation of neuron D180. Recording was made with a 6-site silicon probe with 25- $\mu\text{m}$  spacing between individual taps. Sites closest to the cell body have a typical waveform, including the presence of the capacitive phase on the deepest recording site (site 1) but less so on the site with the strongest recording, presumably closest to the soma (site 2). In the shallower sites in the *stratum oriens* (4–6) the waveform is of smaller amplitude and the  $\text{Na}^+$  phase of the waveform has longer duration (see *Electrode position and width of  $\text{Na}^+$  phase*). Two recording sites, most distant from the cell (5–6), show unusual waveforms similar to a letter “W” in appearance. B: membrane potential and current for the axon and indicated compartments of dendrite 1. AP initiates in dendrite 1 and the axon before invading the soma. First negative peak in the W waveform results from the influx of current into dendrite 1 at initiation. C: membrane potential and current for the soma and indicated compartments of dendrite 2. AP invades the soma from both the axon and dendrite 1 and then spreads to dendrite 2. Current profile in the basal dendrite (first 2 rows, 2nd column) exhibits a large capacitive dominant phase that creates the “notch” in the W shape when superimposed on the negative potential generated by  $\text{Na}^+$  current in dendrite 1, the axon and the soma. Second negative peak of the W is the  $\text{Na}^+$ -dominant phase in dendrite 2 (2nd row, 2nd column). D: extracellular potential waveforms in a transverse section 10  $\mu\text{m}$  caudal to the soma and apical trunk (i.e., soma is at  $z = -10 \mu\text{m}$ , with respect to the plane of the EAPs). Assumed position of the recording electrode is indicated (dotted line). “W” waveform results when a recording site is close to the basal dendrite ( $<20 \mu\text{m}$ ) where the AP initiates and also to a second to dendrite to which the AP backpropagates.

tude) “W” waveform at a proximal site, which we have not been able to reproduce in the model.<sup>1</sup>

## DISCUSSION

Our main finding is that a detailed compartmental model combined with the LSA can accurately reproduce both the waveform and amplitude of recorded EAPs. Further, the model provides precise explanations for many of the features observed experimentally in EAPs. Despite the high degree of variability typical of biological measurements, the complexity of the system under investigation (a single, highly nonlinear nerve cell embedded into nonuniform neuronal tissue), the remoteness of distal dendritic events, and uncertainty about the exact electrode position, our model yields <10% average normalized error (Table 1). This reasonably close match validates the simplified assumptions we made to describe the extracellular milieu in our domain of interest (i.e., at frequencies <3 kHz) using ohmic but no capacitive components. It is known that action potentials in CA1 tend to fire in synchrony with local field potential (LFP) oscillations (Csicsvari et al. 1999). As a result, the EAP waveforms do in fact seem to contain an average LFP component of a few (typically <10) microvolts. These factors may significantly increase the error in matching low-amplitude EAPs.

### Variability of conductance density

An important observation of the present experiments is that exact channel distributions, rather than the details of the dendritic arbors, are the main determinants of the EAP waveform. The implication of this finding is that CA1 pyramidal cells that are usually regarded as a homogeneous set of neurons do have substantial variability in their biophysical properties and that such variability may be identified with proper analysis of the extracellularly recorded spikes.

We demonstrated that for neurons to produce significantly different EAP waveforms in the perisomatic region, it is necessary for the net current profiles in the soma and proximal dendrites to be different, and that the source of this difference is most likely a varied balance of repolarizing K<sup>+</sup> currents. We assumed that variability of the K<sup>+</sup> current contributions made by different ionic current types on different cells is attributable solely to differences in conductance densities (i.e., ionic channel densities) and not to variability in channel behaviors (i.e., kinetics). However, it is known that the activation curves of some ionic channels may shift by several millivolts under various conditions in slice preparations (e.g., LTP; Frick et al. 2004). It seems possible that if we allowed the kinetics of ion current activation/inactivation to vary from cell to cell, we could match the simultaneous intra- and extracellular recordings with less variability in the conductance density levels.

In this light, we consider the choice to fix active current kinetics to be a pragmatic decision based on the need to manage the complexity of the model. In fact, several other important aspects of ionic current behavior were also effectively “lumped” into the conductance density. For example,

Na<sup>+</sup> channels and K and D type K<sup>+</sup> channels in CA1 pyramidal cells are all known to undergo slow, activity-dependent inactivation (Colbert et al. 1997; Klee et al. 1995; Storm 1988). Because an average recording is modeled with a single simulated spike, what may in fact be slow inactivation of these channels is represented in the model as a reduced peak conductance density level. Similarly, the activity of the  $I_{K+C}$  current is strongly dependent on the intracellular [Ca<sup>2+</sup>], which may vary from cell to cell in real neurons but does not vary in the model. Consequently, what may in fact be variations in [Ca<sup>2+</sup>] are also reflected in the model as differences in the density of the  $I_{K+C}$  conductance. Finally, a variety of neuromodulators affect the activation and inactivation of ionic channels in pyramidal neurons (for review see, e.g., Tsubokawa 2000). Any impacts of these various factors are all folded into the parameter controlling the peak conductance density. Consequently, we consider conductance density as a single parameter that actually reflects a large number of factors contributing to the currently available number of any particular ionic channel and not only the absolute number of ionic channels present in the membrane.

### Extracellular recording as a model constraint

We performed extensive and laborious manual and automated tuning of the peak conductance densities to minimize the error between the model and the recordings. However, these results do not prove that we have found a globally optimal solution for all of the parameters. In particular, we have not exhaustively searched the large number of parameters controlling the kinetics of ionic current activation and inactivation. Even without relaxing our assumption that active current kinetics are constant across different cells, it may be that an alternative formulation of the channel kinetics may provide a better match to the recording data.

Although the example of Fig. 4 is admittedly contrived, it suggests that EAPs have been an underutilized resource for constraining compartmental models. Combining extracellular recordings with intracellular recordings is a useful technique, even for in vitro physiology experiments, because it will add precision to the analysis of events involving active ionic currents. If the general properties of the IAP are known for a given cell class (i.e., typical amplitude and duration), then EAP measurements alone may provide sufficient information for constraining a compartmental model to match a specific experimental protocol. In turn, this feature may provide a useful technique for studying the properties of active ionic currents in vivo.

### Impact of cell morphology on EAP

Our results predict that, although sizes of the soma and proximal dendrites constitute an important factor determining the amplitude of the EAP, the details of cell morphology make relatively little impact on the EAP waveform. However, a few caveats apply to this result: In the example of Fig. 6, not only the conductance densities but also the axonal and spine properties appropriate to a CA1 pyramidal cell were mapped onto a basket neuron. This is inexact because basket cells are spineless and have unmyelinated axons. A spineless cell with an unmyelinated axon would have significantly different input

<sup>1</sup> This is recording D188. As can be seen in Table 1 the model match to this recording has the highest error for any extracellular recording. Without this single recording the average error in the match to the EAP recordings would be 8.1% rather than 9.8%.



resistance and AP initiation properties compared with those of a pyramidal cell. To simulate such a cell the conductance density parameters that were tuned to match a pyramidal cell would need to be significantly modified to produce a stable action potential—let alone a particular EAP waveform—which is the reason we have used the pyramidal cell properties for this illustrative example. Therefore the example shows only that the shape of the soma and the location and size of the dendrites do not have an important impact on the EAP, but does not suggest that other properties of specific cell types will not be significant. Also, we have not ruled out the possibility that the cell morphology may be indirectly related to the shape of the EAP waveform by a feedback mechanism through which morphological details control the conductance density levels.

### Pattern of AP initiation

Our results simulating W-shaped waveforms suggest that in specific circumstances the pattern of action potential initiation can be reflected in the EAP. In the simulation of Fig. 7 the dendritic AP initiation was caused by higher input resistance in one dendrite under conditions of uniform dendritic stimulation. However, it is plausible that, *in vivo*, different patterns of dendritic initiation may result from the precise pattern of synaptic input to different dendrites. Alternatively, if the active current conductance densities were significantly different in two dendrites, a similar result may follow (our model always assumed identical properties for all apical and all basal dendrites in a given cell). Consequently, monitoring EAPs may provide insights into the pattern of AP initiation *in vivo*. Initial experiments simulating the waveform of interneurons suggest that similar W-shaped EAPs may be generated when the axon extends from a proximal dendrite (Martina et al. 2000); in that situation the two negative peaks of the waveform are generated by the AP initiation in the axon that then spreads to the soma, but separated by propagation through a connecting dendrite. However, our failure to reproduce one W-shaped waveform in our recording set suggests that there may be other causes for the phenomena.

### Expected developments

Because the model accurately predicts the amplitude of the EAP, we can use it to predict the distance at which an electrode would detect cells not only in the hippocampus but also in other brain regions, where sufficient data are available to constrain the model. Our LSA method is currently being applied to investigate the relative importance of different factors in determining at what distance EAPs may be detected by a recording electrode and to analyze how sampling bias arising from cell size may influence EAP recordings.

To date, extracellular unit recordings have been used mainly to monitor the spike output of neurons. However, multiple-site high-resolution extracellular recordings can also provide useful information about intracellular features of the recorded neurons. For example, the extent of somadendritic backpropagation of action potentials can be monitored in the intact brain as a function of behavior (e.g., Buzsáki et al. 1996; Quirk et al. 2001). Our findings suggest that accurate and high-resolution monitoring of EAP can provide information about alteration of conductance densities in single neurons as a function of state

changes and plasticity. Because subcortical neuromodulators and use-dependent activation of neurons are known to modulate the various conductances, our results imply that by monitoring the waveforms, EAPs can provide access to this valuable information in behaving animals. Finally, models consisting of large numbers of geometrically arranged neurons can provide the needed tool for the perfection of unit-classifying algorithms and to the development of ideal recording electrode configurations without the need of simultaneous extracellular and intracellular recordings from various cell types and brain regions.

## APPENDIX

### A. Passive parameters and spines

Spines are accounted for by adjusting the passive membrane parameters only for spiny compartments according to a folding factor  $f$ , similar to that described in Major et al. (1994). But here we modify the passive properties of the compartment directly without modifying the compartment length or diameter as that would also impact the properties of active ionic currents. That is

$$f = A_s/A_c$$

$$C_m = C_m(1 + f)$$

$$R_m = R_m/(1 + f)$$

where  $A_s$  is the estimated spine surface area for the compartment and  $A_c$  is the actual surface area of the compartment derived from the histological reconstruction that ignores spines.  $A_s$  is given by

$$A_s = L \times \delta \times \alpha$$

where  $L$  is the length of the compartment (in m),  $\delta$  is the density of spines at the compartment location (in spines/ $\mu\text{m}$ ), and  $\alpha$  is the average area of a spine, assumed to be  $0.83 \mu\text{m}^2$  (Harris and Stevens 1989). The spine densities ( $\delta$ ) used in the model are specific to different sections of the cell as described in Megias et al. (2001). The classification of compartments to the categories described in Megias et al. (2001) was based on the compartment diameter ( $d$ ) and path distance from the soma ( $\Delta$ ). Both the spine densities and criteria for compartmental classification are listed in Table A1.

TABLE A1. Spine model parameters

Region, Type	$\delta$ , spines/ $\mu\text{m}$	Compartment Classification*	
		Distance	Diameter
oriens, proximal	0.64	$\Delta < 50$	All basal
oriens, distal	3.4	$\Delta > 50$	All basal
radiatum, thick proximal	0.03	$\Delta \leq 50$	$d > 1.5$
radiatum, thick medial	2.3	$50 < \Delta < 150$	$d > 1.5$
radiatum, thick distal	6.9	$\Delta \geq 150$	$d > 1.5$
radiatum, thin	3.5	$\Delta \leq 300$	$d < 1.5$
lacunosum-moleculare, thick	1.72	$\Delta > 300$	$1 < d < 1.5$
lacunosum-moleculare, medium/thin†	0.6	$\Delta > 300$	$d \leq 1$

Variable parameters for the spine model of APPENDIX A. \*All units are in micrometers ( $\mu\text{m}$ ). †Represents an average of the values for lacunosum-moleculare/medium and lacunosum-moleculare/thin from Megias et al. (2001).

TABLE B1. Parameters for non- $\text{Ca}^{2+}$ -dependent current kinetics

Current	Variable	Order	$V_{1/2}$ , mV	$z$	$\gamma$	$K$ , 1/ms	$\tau_0$ , ms
$I_{\text{Na}^+ \text{Ax}}$	$m$	3	-51	-4.6	.05	100	0.04
	$h$	1	-50	12.6	0.2	2	0.25
$I_{\text{Na}^+ \text{SD}}$	$m$	3	-46	-4.2	.05	100	0.04
	$h$	1	-50	12.6	0.2	1.33	0.25
$I_{\text{HSoma}}$	$m$	1	-82	6.3	—	—	100
$I_{\text{HDend}}$	$m$	1	-90	6.3	—	—	100
$I_{\text{K}^+ \text{AProx}}$	$m$	4	-40	-3.2	—	—	0.2
	$h$	2	-50	3.2	0.5	0.67	0.3
$I_{\text{K}^+ \text{ADist}}$	$m$	4	-50	-3.2	—	—	0.2
	$h$	2	-60	3.2	0.5	0.67	0.3
$I_{\text{K}^+ \text{D}}$	$m$	4	-63	-3	0.5	1.00	0.25
	$h$	2	-73	2.5	0.5	—	1,000
$I_{\text{K}^+ \text{K}}$	$m$	1	-5	-5.1	0.5	0.25	0.25
	$h$	1	-65	1.7	0.5	1	100
$I_{\text{K}^+ \text{M}}$	$m$	2	-45	-6.3	0.5	0.5	2
$I_{\text{Ca}^{2+} \text{L}}$	$m$	2	5	-3.2	0.5	0.5	2
$I_{\text{Ca}^{2+} \text{N}}$	$m$	2	-14	-3.9	0.2	0.2	1
	$h$	1	-40	2.5	0.5	1	50
$I_{\text{Ca}^{2+} \text{R}}$	$m$	2	0	-3.2	0.5	0.33	3
	$h$	1	-40	2.8	0.5	1	50
$I_{\text{Ca}^{2+} \text{T}}$	$m$	2	-30	-3.6	0.1	0.2	2
	$h$	1	-60	5.1	0.5	1	25

Parameter values for non- $\text{Ca}^{2+}$ -dependent active current kinetics, using the formalism described in Borg-Graham (1999). Note that for all current types activation particles are denoted  $m$  and inactivation particles are denoted  $h$ .

### B. Ionic current model kinetics

The formalism used for the active current models is that described in Borg-Graham (1999).<sup>2</sup> The parameters for the kinetics of non- $\text{Ca}^{2+}$ -dependent currents are listed in Table B1. There are many differences between the parameter values determined by Borg-Graham (1999) and the values we have chosen for the model of simultaneous in vivo intra- and extracellular recordings. Perhaps the most important differences are the significantly faster time course of activation used for the primary  $\text{K}^+$  currents active in repolarization,  $I_{\text{K}^+ \text{AProx}}$ ,  $I_{\text{K}^+ \text{ADist}}$ ,  $I_{\text{K}^+ \text{C}}$ ,  $I_{\text{K}^+ \text{D}}$ ,  $I_{\text{K}^+ \text{K}}$ , and  $I_{\text{K}^+ \text{M}}$ . As described earlier in Active current conductance density and the EAP waveform, these changes were required to match the variety of extracellular potential waveforms. Other differences between the two models have lesser significance, such as the differences between the properties of  $\text{Ca}^{2+}$  currents.

For the  $\text{Ca}^{2+}$ -dependent currents,  $I_{\text{K}^+ \text{C}}$  and  $I_{\text{K}^+ \text{AHP}}$  we adopt the Markov model formalism, also from Borg-Graham (1999). The parameters used are listed in Tables B2 and B3. We have again changed the model parameters to match the simultaneous intra- and extracellular recordings by speeding up the activation speeds and increasing the sensitivity of the channels to changes in the  $\text{Ca}^{2+}$  concentration.

For calcium buffering and diffusion we used the Cadifus mechanism included with NEURON (Hines and Carnevale 2001). The mechanism models  $\text{Ca}^{2+}$  diffusion in four concentric cells for all compartments. The rates of buffering and diffusion have been adapted to approximately match the results described in Jaffe et al. (1994) and Christie et al. (1995): the average  $\text{Ca}^{2+}$  concentration in the central shells is on the order of 50–100 nM, and a single action potential increases the concentration by 2–10 nM. To achieve these results we altered the parameter for the initial calcium concentration ( $\text{cai}$ ) from 50 to 75 nM to model a cell that has been recently active, although we simulated only a single action potential. We also changed the Total Buffer concentration parameter from 3 to 5 nM and the forward buffering rate ( $k1\text{Buf}$ ) from 100 to 250/mM-ms.

<sup>2</sup> The one exception is the  $\text{Na}^+$  channel for which Borg-Graham (1999) did not use the Hodgkin-Huxley type formalism.

TABLE B2. Parameters for  $I_{\text{K}^+ \text{AHP}}$  current kinetics

Variable	Order	$\alpha$ , $\text{ms}^{-1} \text{mM}^{-n}$	$\beta$ , 1/ms	$n$	$\tau_0$ , ms
$m$	8	$1\text{e}31$	0.2	2	5

Parameters for the  $I_{\text{K}^+ \text{AHP}}$  current model using the formalism described in Borg-Graham (1999).

### C. Active ion current model conductance densities

Several active currents in the model had nonuniform conductance density distributions in the compartmental model. Although the properties of all of the ion currents are studied primarily in the soma and thick apical dendrites we have assumed similar properties occur in basal dendrites. The general approach is similar to that described in Poiraszi et al. (2003) and the precise distributions used are described below. Current types not listed had a uniform density in every compartment. The peak conductance densities used for each cell along with parameters used to define the nonuniform densities are listed in Tables C1, C2, and C3. Densities for the currents that were held constant for all cells are listed in Table C4.

1)  $I_{\text{Na}^+ \text{Ax}}$ : The density at the axon initial segment and at nodes of Ranvier is a small multiple ( $<5$ ) of the density on the soma,  $g_{\text{init-seg}} = g_{\text{soma}} \times \alpha_{\text{init-seg}}$ ;  $g_{\text{node}} = g_{\text{soma}} \times \alpha_{\text{node}}$  (Colbert and Pan 2002). The values used for  $\alpha_{\text{node}}$  and  $\alpha_{\text{init-seg}}$  were varied for each cell to match the simultaneous intra- and extracellular recordings, as listed in Table C1.

2)  $I_{\text{Na}^+ \text{SD}}$ : The density is the same on the soma and axon hillock (Colbert et al. 1996) and the current is subject to slow inactivation, which tends to increase with distance from the soma (Colbert et al. 1997). Peak conductance density in dendritic compartments is defined as a percentage of the somatic density with a linear decrease from the proximal dendrites to distal dendrites.

The conductance density for a given compartment is defined by the equation:  $g_{\text{dendrite}} = g_{\text{soma}} \times \{\gamma_{\text{min}} + [\gamma_{\text{max}} - \gamma_{\text{min}}] \times [(300 - \Delta)/300]\}$ , where  $\gamma_{\text{max}}$  and  $\gamma_{\text{min}}$  indicate the maximum dendritic conductance density ratio (in the proximal dendrites) and the minimum dendritic conductance density ratio (in the distal dendrites), respectively;  $\Delta$  is the path distance from the soma to the compartment; and 300  $\mu\text{m}$  is the distance at which the conductance density reaches its minimum. At distances  $>300 \mu\text{m}$  the conductance density for all compartments is given by  $g_{\text{soma}} \times \gamma_{\text{min}}$ . The values used for  $\gamma_{\text{max}}$  and  $\gamma_{\text{min}}$  were varied for each cell to match the simultaneous intra- and extracellular recordings, as listed in Table C1.

3)  $I_{\text{K}^+ \text{AProx/Dist}}$ : The conductance density for currents in distal dendrites are significantly higher and exhibit shifted activation kinetics to be more active at lower voltage. Because of their low activation threshold, a nontrivial fraction of these channels are active at rest. Results in Frick et al. (2003) suggest that there are even higher conductance densities for these current in narrow dendrites off the apical trunk and we found this assumption consistent with reproducing the simultaneous intra- and extracellular recordings. In the proximal dendrites closer than 100  $\mu\text{m}$  to the soma, the  $I_{\text{K}^+ \text{AProx}}$  current has a fixed conductance density. In the distal dendrites, the  $I_{\text{K}^+ \text{ADist}}$  current replaces the  $I_{\text{K}^+ \text{AProx}}$  current, and the peak conductance density increases linearly with distance from the soma. The peak

TABLE B3. Parameters for  $I_{\text{K}^+ \text{C}}$  current kinetics

Transition	$1/\tau_{\text{max}}$ , 1/ms	$k$ , mV	$V_{1/2}$ , mV	$1/\tau_{\text{min}}$ , 1/ms	$\alpha \text{ mM}^{-n}$	$n$
$\text{O} \rightarrow \text{I}$	0	12	-30	0.67	—	—
$\text{I} \rightarrow \text{C}$	0	-10	-120	10	—	—
$\text{C} \rightarrow \text{O}$	0.02	6	-45	50	$2.50\text{E}+10$	3
$\text{O} \rightarrow \text{C}$	0	-3	-40	0.67	—	—

Parameters for the  $I_{\text{K}^+ \text{C}}$  current model using the formalism described in Borg-Graham (1999).

TABLE C1. Conductance density parameters for  $Na^+$  current

Cell	$g_{soma}$	Apical		Basal		$\alpha_{node}$	$\alpha_{iseg}$
		$\gamma_{min}$	$\gamma_{max}$	$\gamma_{min}$	$\gamma_{max}$		
D037	45	0.5	0.8	0.3	0.71	3.0	2
D056	35	0.1	0.51	0.31	0.72	3.0	4
D068	35.3	0.2	0.41	0.3	0.71	2.0	1.5
D081	33	0.3	0.7	0.32	0.7	3.0	3
D112.1	30	0.7	0.9	0.7	0.87	3.0	2
D112.2	28.3	0.56	1.02	0.78	1.03	3.1	2
D128	39.1	0.3	0.6	0.5	0.94	3.0	2
D135	42	0.3	0.53	0.3	0.69	3.0	2
D137	40.8	0.81	0.95	0.3	0.65	3.0	1.9
D145	40	0.3	0.7	0.3	0.71	3.0	3
D147	25.1	0.35	0.7	0.76	1.06	3.0	2
D149	25.2	0.75	0.75	0.55	0.95	3.0	2
D151	50.1	0.15	0.86	0.05	0.85	1.0	1
D163	35	0.3	0.86	0.51	1	3.0	2
D180	38	0.3	0.35	0.9	1	1.5	1.1
D187	43.8	0.1	0.5	0.1	0.5	2.0	5
D188	40	0.7	0.9	0.7	0.9	3.0	2
D189	25	0.42	0.9	0.4	0.5	3.0	1.5
Average	36.1	0.4	0.72	0.45	0.8	2.7	2.2
SD	7.3	0.22	0.2	0.24	0.17	0.6	1

Units for  $g$  are  $mS/cm^2$ . Other quantities are dimensionless.

conductance density in a given distal trunk compartment is defined by the equation:  $g_{dendrite} = g_{distal} \times \{1 + 6 \times [(\Delta - 100)/(350 - 100)]\}$ , where  $g_{distal}$  defines the initial density for distal dendrites, the factor of 7 defines the ratio of the maximum conductance density (in the far distal dendrites) to the minimum conductance density (in the near distal dendrites), 100  $\mu m$  is the maximum distance considered to be proximal, and 350  $\mu m$  is the distance from the soma at which the conductance density reaches the maximum value. For compartments further than 350  $\mu m$  the conductance density is fixed at  $g_{dendrite} = g_{distal} \times 7$ . In narrow dendrites (basal, apical oblique, and apical tuft) the peak conductance density is boosted by a further multiplicative factor over whatever the conductance density would be in a similar thick dendrite. That is, the distal conductance density in narrow

TABLE C2. Conductance density parameters for A, D, K, and M type  $K^+$  currents

Cell	$I_{K^+AProx}$ $g$	$I_{K^+ADist}$				$I_{K^+D}$ $g$	$I_{K^+K}$ $g$	$I_{K^+M}$ $g$
		$g$	$\alpha_{basal}$	$\alpha_{oblique}$	$\alpha_{tuft}$			
D037	25	41.9	2	2	3	0.5	49.9	0.5
D056	7	9.8	2	2	3	0.5	1	0.7
D068	10.1	9.7	3	3	4	1	49.9	0.7
D081	5	5	2	2	3	1	8	0.9
D112.1	35	35	5	4	6	1	1.5	1
D112.2	2.5	20.2	3	3	4.9	0.5	0.5	0.5
D128	9.9	11.1	2	2	3	1	9	0.2
D135	10.3	15.2	2	3.1	4	4	8.3	0.5
D137	5.1	4.8	3.1	2	3	4	70.6	1.5
D145	15	24.9	3	3	4	0.5	3	0.8
D147	2.5	21	3	3	4	0.5	0.5	0.8
D149	2.5	22	1	3	4	0.5	0.5	0.3
D151	5	8	3	3	5	2	12	0.2
D163	7.5	12.6	2	2	3	0.5	14.6	0.8
D180	10	47	2	2	3	1	0.5	0.5
D187	5	10.7	2	2	3	1	10	1
D188	41.2	40.1	2	2	3	2	0.5	0.5
D189	2.5	22.5	2.6	2	3	0.5	0.5	0.5
Average	11.2	20.1	2.5	2.5	3.7	1.2	13.4	0.7
SD	11.3	13.1	0.9	0.6	0.9	1.1	20.9	0.3

Units for  $g$  are  $mS/cm^2$ . Other quantities are dimensionless.

TABLE C3. Conductance density parameters for C type  $K^+$  current

Cell	$g_{soma}$	Apical		Basal	
		$\alpha$	$\Delta_{prox}$	$\alpha$	$\Delta_{prox}$
D037	1	0.75	100	0.75	50
D056	10	0.97	100	0.75	100
D068	1	0.75	25	0.76	25
D081	12	0.75	50	0.76	50
D112.1	3	0.75	50	0.75	50
D112.2	8.9	1.0	99	0.74	99
D128	22.1	0.75	150	0.75	99
D135	5.9	1.0	101	0.78	97
D137	30.4	0.76	101	0.76	50
D145	9	1.0	75	0.78	50
D147	19.9	0.99	99	0.76	99
D149	25.6	1.0	50	1.0	101
D151	13.5	1.0	126	0.5	101
D163	6.1	0.98	101	1.01	101
D180	12	0.25	50	0.75	100
D187	8	0.5	50	0.75	100
D188	40	0.25	25	1.0	100
D189	7.5	0.75	100	0.75	50
Average	13.1	0.79	81	0.78	79
SD	10.6	0.24	35	0.12	27

Units for  $g$  are  $mS/cm^2$ . Other quantities are dimensionless.

dendrites is given by  $g_{narrow-dendrite} = g_{dendrite} \times \alpha_{basal/oblique/tuft}$ . The values used for  $\alpha_{basal}$ ,  $\alpha_{oblique}$ , and  $\alpha_{tuft}$  were varied for each cell to match the simultaneous intra- and extracellular recordings. The values used are listed in Table C2.

4)  $I_{K^+C}$ : This current has a high conductance density and contributes to repolarization in the soma and proximal dendrites only (Poolos and Johnston 1999). Density of the  $I_{K^+C}$  current is greatest at the soma and declines to zero outside of the proximal dendrites. The conductance density for compartments within the proximal dendrites is given by the equation  $g_{proximal} = g_{soma} \times \alpha \times [(\Delta - \Delta_{prox})/(\Delta_{prox})]$ , where  $\Delta$  is the path distance from the soma to the compartment,  $\Delta_{prox}$  is the maximum distance from the soma considered to be proximal, and  $\alpha$  ( $1 \geq \alpha$ ) defines the maximum conductivity density in the proximal dendrites. For compartments further from the soma than  $\Delta_{prox}$  the conductance density of the  $I_{K^+C}$  current is zero. The values used for  $\alpha$  and  $\Delta_{prox}$  were independently varied in the apical and basal dendrites for each cell to match the simultaneous intra- and extracellular recordings. The values used are listed in Table C3.

5)  $I_{HSoma/Dend}$ : The conductance density of this current is greatest in the distal dendrites, where the activation requires somewhat more hyperpolarized potentials. The conductance density of  $I_{HDend}$  current is defined as a multiple of the  $I_{HSoma}$  conductance density, with the multiplicative factor increasing linearly with distance from the soma. For a dendritic compartment the conductance density of  $I_{HDend}$  current is defined by the equation  $g_{dendrite} = g_{soma} \{1 + 6 \times [1 - ((300 - \Delta)/300)]\}$ , where 1 and 6 are ratios defining the minimum (proximal) and maximum (distal) density of  $I_{HDend}$  in relation to  $I_{HSoma}$ ;  $\Delta$  is the path distance from the soma to a given compartment; and 300  $\mu m$  is the distance at which the  $I_{HDend}$  conductance reaches its maximum

TABLE C4. Conductance density parameters for AHP type  $K^+$  currents,  $Ca^{2+}$  currents, and H type currents

	$I_{K^+AHP}$		$I_{Ca^{2+}L}$		$I_{Ca^{2+}N}$ $g$	$I_{Ca^{2+}R}$ $g$	$I_{Ca^{2+}T}$ $g$	$I_{HSoma}$ $g$
	$g_{high}$	$g_{low}$	$g_{high}$	$g_{low}$				
All cells	0.1	0.05	0.2	0.02	0.2	0.2	0.1	0.4

Units for  $g$  are  $mS/cm^2$ .



density. For compartments at distances  $>300\ \mu\text{m}$  from the soma, the density is fixed at  $g_{\text{soma}} \times 7$ .

6)  $I_{K^+ \text{AHP}}$ : This current is located in dendrites only. The conductance density of  $I_{K^+ \text{AHP}}$  is highest in the proximal dendrites and lower in distal dendrites. For dendrites with a distance  $\Delta < 100\ \mu\text{m}$  the conductance density is set to  $g_{\text{high}}$ , whereas for dendrites with distance  $\Delta \geq 100\ \mu\text{m}$  the conductance density is set to  $g_{\text{low}}$  (listed in Table C4).

7)  $I_{Ca^{2+}L}$ : This current is located in dendrites only. The conductance density of  $I_{Ca^{2+}L}$  is highest in the proximal dendrites and lower in distal dendrites. For dendrites with a distance  $\Delta < 50\ \mu\text{m}$  the conductance density is set to  $g_{\text{high}}$ , whereas for dendrites with distance  $\Delta \geq 50\ \mu\text{m}$  the conductance density is set to  $g_{\text{low}}$  (listed in Table C4).

8)  $I_{Ca^{2+}T}$ : This current is located in dendrites only and has a conductance density that increases with distance from the soma. For a dendritic compartment the conductance density is given by the equation  $g_{\text{dendrite}} = g_{\text{distal}} \times (\Delta/150)$ , where  $g_{\text{distal}}$  is the maximum conductance density in distal dendrites,  $\Delta$  is the path distance from the soma to the compartment, and  $150\ \mu\text{m}$  is the distance from the soma at which the conductance density reaches its peak value. For compartments with  $\Delta \geq 150\ \mu\text{m}$  the conductance density  $g_{\text{dendrite}} = g_{\text{distal}}$ .

9)  $I_{Ca^{2+}N/R}$ :  $Ca^{2+}$  currents of the N and R type are located in the soma only. The density is zero in dendritic compartments.

#### ACKNOWLEDGMENTS

We thank D. Robbe for providing extracellular recordings for comparison with the simultaneous intra- and extracellular recordings and Tim Barnes for validation of the inhomogeneous resistivity calculation.

#### GRANTS

This work was supported by National Institute of Mental Health (NIMH) Fellowship 1-F31-MH-070144-01A1 and Grant MH-12403, National Institute of Neurological Disorders and Stroke Grants NS-34994 and NS-43157, the NIMH-supported Conte Center for the Detection and Recognition of Objects, and the National Science Foundation.

#### REFERENCES

- Borg-Graham LJ. Interpretations of data, mechanisms for hippocampal pyramidal cell models. In: *Cerebral Cortex 13*, edited by Ulinksi PS, Jones EG, and Peters A. New York: Plenum Press, p. 19–138.
- Buzsáki G and Kandel A. Somadendritic backpropagation of action potentials in cortical pyramidal cells of the awake rat. *J Neurophysiol* 79: 1587–1591, 1998.
- Buzsáki G, Penttonen M, Nadasdy Z, and Bragin A. Pattern, inhibition-dependent invasion of pyramidal cell dendrites by fast spikes in the hippocampus in vivo. *Proc Natl Acad Sci USA* 93: 9921–9925, 1996.
- Christie BR, Eliot LS, Ito K, Miyakawa H, and Johnston D. Different  $Ca^{2+}$  channels in soma, dendrites of hippocampal pyramidal neurons mediate spike-induced  $Ca^{2+}$  influx. *J Neurophysiol* 73: 2553–2557, 1995.
- Colbert CM and Johnston D. Axonal action-potential initiation,  $Na^+$  channel densities in the soma, axon initial segment of subicular pyramidal neurons. *Neuroscience* 16: 6676–6686, 1996.
- Colbert CM, Magee JC, Hoffman DA, and Johnston D. Slow recovery from inactivation of  $Na^+$  channels underlies the activity-dependent attenuation of dendritic action potentials in hippocampal CA1 pyramidal neurons. *Neuroscience* 17: 6512–6521, 1997.
- Colbert CM and Pan E. Ion channel properties underlying axonal action potential initiation in pyramidal neurons. *Nat Neurosci* 5: 533–538, 2002.
- Csicsvari J, Henze DA, Jamieson B, Harris KD, Sirota A, Bartho P, Wise KD, and Buzsáki G. Massively parallel recording of unit, local field potentials with silicon-based electrodes. *J Neurophysiol* 90: 1314–1323, 2003.
- Csicsvari J, Hirásé H, Czurko A, Mamiya A, and Buzsáki G. Oscillatory Coupling of Hippocampal, pyramidal cells, interneurons in the behaving rat. *Neuroscience* 19: 274–287, 1999.
- Destexhe A and Paré D. Impact of network activity on the integrative properties of neocortical pyramidal neurons in vivo. *J Neurophysiol* 81: 1531–1547, 1999.
- Fisher RE, Gray R, and Johnston D. Properties, distributions of single voltage-gated calcium channels in adult hippocampal neurons. *J Neurophysiol* 64: 91–104, 1990.
- Frick A, Magee J, and Johnston D. LTP is accompanied by an enhanced local excitability of pyramidal neuron dendrites. *Nat Neurosci* 7: 126–135, 2004.
- Frick A, Magee J, Koester HJ, Migliore M, and Johnston D. Normalization of  $Ca^{2+}$  signals by small oblique dendrites of CA1 pyramidal neurons. *Neuroscience* 23: 3243–3250, 2003.
- Gray CM, Maldonado PE, Wilson M, and McNaughton B. Tetrodes markedly improve the reliability, yield of multiple single-unit isolation from multi-unit recordings in cat striate cortex. *J Neurosci Methods* 63: 43–54, 1995.
- Gulyas AI, Megias M, Emri Z, and Freund T. Total number and ratio of excitatory synapses converging into single interneurons of different types in the CA1 area of rat hippocampus. *Neuroscience* 19: 10082–10097, 1999.
- Halliwel JV and Adams PR. Voltage-clamp analysis of muscarinic excitation in hippocampal neurons. *Brain Res* 250: 71–92, 1982.
- Harris KM and Stevens JK. Dendritic spines of CA1 pyramidal cells in the rat hippocampus: serial electron microscopy with reference to their biophysical characteristics. *Neuroscience* 9: 2982–2997, 1989.
- Henze DA, Borhegyi Z, Csicsvari J, Mamiya A, Harris K, and Buzsáki G. Intracellular features predicted by extracellular recordings in the hippocampus in vivo. *J Neurophysiol* 83: 390–400, 2000.
- Henze DA and Buzsáki G. Action potential threshold of hippocampal pyramidal cells in vivo is increased by recent spiking activity. *J Neurosci Methods* 105: 121–130, 2001.
- Hines ML and Carnevale NT. The neuron simulation environment. *Neural Comput* 9: 1179–1209, 1997.
- Hines ML and Carnevale NT. Expanding NEURON's repertoire of mechanisms with NMODL. *Neural Comput* 12: 995–1007, 2000.
- Hines ML and Carnevale NT. NEURON: a tool for neuroscientists. *Neuroscientist* 7: 123–135, 2001.
- Hoffman DA, Magee JC, Colbert CM, and Johnston D.  $K^+$  channel regulation of signal propagation in dendrites of hippocampal pyramidal neurons. *Nat Neurosci* 387: 869–875, 1997.
- Holt G. *A Critical Reexamination of Some Assumptions, Implications of Cable Theory in Neurobiology* (PhD Thesis). Pasadena, CA: Program in Computation and Neural Systems, California Institute of Technology, 1998.
- Holt G and Koch C. Electrical interactions via the extracellular potential near cell bodies. *J Comput Neurosci* 6: 169–184, 1999.
- Jaffe DB, Ross WN, Lisman JE, Lasser-Ross N, Miyakawa H, and Johnston D. A model for dendritic  $Ca^{2+}$  accumulation in hippocampal pyramidal neurons based on fluorescence imaging measurements. *J Neurophysiol* 71: 1065–1077, 1994.
- Kamondi A, Acsády L, and Buzsáki G. Dendritic spikes are enhanced by cooperative network activity in the intact hippocampus. *J Neuroscience* 18: 3919–3928, 1998.
- Klee R, Ficker E, and Heinemann U. Comparison of voltage-dependent potassium currents in rat pyramidal neurons acutely isolated from hippocampal regions CA1, CA3. *J Neurophysiol* 74: 1982–1995, 1995.
- Koch C. *Biophysics of Computation*. Oxford, UK: Oxford Univ. Press, 1999.
- Koch C and Segev I. (Editors). *Methods in Neuronal Modeling: From Ions to Networks*. Cambridge, MA: Bradford, 1999.
- Lancaster B and Nicoll RA. Properties of two calcium-activated hyperpolarizations in rat hippocampal slices. *J Physiol* 389: 187–203, 1987.
- López-Aguado L, Ibarz JM, and Herrerías O. Activity-dependent changes of tissue resistivity in the CA1 region in vivo are layer specific: modulation of evoked potentials. *J Neurosci Methods* 108: 249–262, 2001.
- Magee JC. Dendritic hyperpolarization-activated currents modify the integrative properties of hippocampal CA1 pyramidal neurons. *Neuroscience* 18: 7613–7624, 1998.
- Magee JC and Johnston D. Characterization of single voltage-gated  $Na^+$ ,  $Ca^{2+}$  channels in apical dendrites of rat CA1 pyramidal neurons. *J Physiol* 487: 67–90, 1995.
- Mainen ZF, Joerges J, Huguenard JR, and Sejnowski TJ. A model of spike initiation in neocortical pyramidal neurons. *Neuron* 15: 1427–1439, 1995.
- Major G, Larkman AU, Jonas P, Sakmann B, and Jack JB. Detailed passive cable models of whole-cell recorded CA3 pyramidal neurons in rat hippocampal slices. *Neuroscience* 14: 4613–4638, 1994.
- Martina M and Jonas P. Functional difference in  $Na^+$  channel gating between fast-spiking interneurons, principal neurones of rat hippocampus. *J Physiol* 505: 593–603, 1997.
- Martina M, Vida I, and Jonas P. Distal initiation and active propagation of action potentials in interneuron dendrites. *Science* 287: 295–300, 2000.
- Maxwell JC. *A Treatise on Electricity, Magnetism*. Oxford, UK: Clarendon Press, 1881.

- Megias M, Emri ZS, Freund TF, and Gulyas AI.** Total number, distribution of inhibitory, excitatory synapse on hippocampal CA1 pyramidal cells. *J Neurosci Methods* 102: 527–540, 2001.
- Moffit MA and McIntyre CC.** Model-based analysis of cortical recording with silicon microelectrodes. *Clin Neurophysiol* 116: 2240–2250, 2005.
- Mountcastle VB, Talbot WH, Sakata H, and Hyvarinen J.** Cortical neuronal mechanisms in flutter-vibration studied in unanesthetized monkeys: neuronal periodicity, frequency discrimination. *J Neurophysiol* 32: 452–484, 1969.
- Plonsey R.** *Bioelectric Phenomena*. New York: McGraw-Hill, 1969.
- Poirazi P, Brannon TM, and Mel BW.** Arithmetic of subthreshold synaptic summation in a model CA1 pyramidal cell. *Neuron* 37: 977–987, 2003.
- Poolos NP and Johnston D.** Calcium-activated potassium conductances contribute to action potential repolarization at the soma but not the dendrites of hippocampal CA1 pyramidal neurons. *Neuroscience* 19: 5205–5212, 1999.
- Quiñan Quiroga R, Nadasdy Z, and Ben-Shaul Y.** Unsupervised spike sorting with wavelets, superparamagnetic clustering. *Neural Comput* 16: 1661–1687, 2004.
- Quirk MC, Blum KI, and Wilson MA.** Experience-dependent changes in extracellular spike amplitude may reflect regulation of dendritic action potential back-propagation in rat hippocampal pyramidal cells. *Neuroscience* 21: 240–248, 2001.
- Rall W.** Electrophysiology of a dendritic neuron model. *Biophys J* 2: 145–167, 1962.
- Rosenfalck P.** Intra- and extracellular potential fields of active nerve and muscle fibres—a physico-mathematical analysis of different models. *Acta Physiol Scand Suppl* 321: 1–168, 1969.
- Spruston N and Johnston D.** Perforated patch-clamp analysis of the passive membrane properties of three classes of hippocampal neurons. *J Neurophysiol* 67: 508–529, 1992.
- Storm JF.** Temporal integration by a slowly inactivating  $K^+$  current in hippocampal neurons. *Nature* 336: 379–381, 1988.
- Stuart G and Spruston N.** Determinants of voltage attenuation in neocortical pyramidal neuron dendrites. *Neuroscience* 18: 3501–3510, 1998.
- Toledo-Rodriguez M, Blumenfeld B, Wu C, Luo J, Attali B, Goodman P, and Markram H.** Correlation maps allow neuronal electrical properties to be predicted from single-cell gene expression profiles in rat neocortex. *Cereb Cortex* 14: 1310–1327, 2004.
- Trayanova N and Henriquez CS.** Modification of a cylindrical bidomain model for cardiac tissue. *Math Biosci* 104: 59–72, 1991.
- Tsubokawa H.** Control of  $Na^+$  spike backpropagation by intracellular signaling in the pyramidal neuron dendrites. *Mol Neurobiol* 1: 129–141, 2000.
- Weber E.** *Electro Magnetic Fields: Theory, Applications*. New York: Wiley, 1950.
- Williamson A and Alger BE.** Characterization of an early afterhyperpolarization after a brief train of action potentials in rat hippocampal neurons in vitro. *J Neurophysiol* 63: 72–81, 1990.
- Wilson MA and McNaughton BL.** Dynamics of the hippocampal ensemble code for space. *Science* 261: 1055–1058, 1993.
- Yoshida A, Oda M, and Ikemoto Y.** Kinetics of  $Ca^{2+}$ -activated  $K^+$  channel in rat hippocampal neurons. *Jpn J Physiol* 41: 297–315, 1991.